Efficient numerical scheme for a dendritic solidification phase field model with melt convection ☆

Chuanjun Chen [a], Xiaofeng Yang [b],*

[a] *School of Mathematics and Information Sciences, Yantai University, Yantai 264005, China*
[b] *Department of Mathematics, University of South Carolina, Columbia, SC 29208, United States of America*

A R T I C L E   I N F O

A B S T R A C T

In this paper, we consider numerical approximations for a dendritic solidification phase field model with melt convection in the liquid phase, which is a highly nonlinear system that couples the anisotropic Allen-Cahn type equation, the heat equation, and the weighted Navier-Stokes equations together. We first reformulate the model into a form which is suitable for numerical approximations and establish the energy dissipative law. Then, we develop a linear, decoupled, and unconditionally energy stable numerical scheme by combining the modified projection scheme for the Navier-Stokes equations, the Invariant Energy Quadratization approach for the nonlinear anisotropic potential, and some subtle explicit-implicit treatments for nonlinear coupling terms. Stability analysis and various numerical simulations are presented.

1. Introduction

In this paper, we consider numerical approximations for a dendritic phase field model to simulate the microstructure evolution in solidification processes that involves melt convections in the liquid phase. The pattern of dendritic growth that develops with a typical multi-branching tree-like form, is often observed in the solidification process of metals or crystallization in supersaturated solutions, see [15,22,25]. Started from the pioneering modeling work of Halperin, Kobayashi, and Collins et al. in [6,20,32], the phase field method or called diffusive interface approach, that is a powerful numerical tool for simulating free interfacial motions, had been widely used in modeling and numerical approaches for the study of the dendritic solidification process, cf. [2,3,5,13,27,29–31,36,40,50,51,64].

In the phase field approach, the solidification front is treated as a moving interface, that is automatically given by the level set of an order parameter (phase field variable) which is adopted to distinguish the physical state (liquid or solid) of the system at each point using distinct values. The free-energy functional of the system incorporates a specific form of the conformational entropy with anisotropic spatial gradients that is introduced to study the dynamics of atomic-scale dendritic crystal growth. If the flow convection in the liquid phase is neglected, the solidification process is then controlled by the interplay of thermal, solutal, capillary, and kinetic length or time scales [49]. For this case, the governing model can be reduced to the nonlinear coupling of two equations, where one is the anisotropic Allen-Cahn type diffusive equation for the

phase field variable, and the other is the second order equation for the latent heat since the crystallization process does involve heat-transfer along the interface. Such a partial model with the absence of flow convection had been widely studied in numerous works, theoretically and numerically, see [29–31,36,40,50,64] and the references therein.

Comparing to the partial model ignoring the flow field, when the melt convection of the liquid phase is considered, the new length and time scales will be added to the problem that results in morphologies which are potentially much different from those generated by purely diffusive heat and solute transport. Moreover, when the flow convection influences the solidification pattern, the evolving microstructure can also bring up unexpected and complicated flow phenomena reciprocally, cf. [1,5,7,8,53]. The full solidification phase field model with flow convections on the microscopic scale was first proposed by Beckerman et al. in [2,48], and had been extensively studied numerically in many subsequent works, see [27,28,33,39,65]. Formally, Beckerman's solidification phase field model (B-SPF) with flow convections consists of three nonlinearly coupled equations: the Allen-Cahn type equation with a gradient-dependent anisotropic coefficient for the phase field variable, the heat transfer equation, and the Navier-Stokes equation for the flow field. Meanwhile, as a matter of fact, the solidification system is a binary mixture of solid and liquid, thus the convection, the fluid velocity, as well as the continuity equation are all needed to be confined on the liquid phase, that is fulfilled by using an artful weighted factor in the B-SPF model.

It is remarkable that, despite a great deal of numerical works to simulate the solidification process, to the best of the author's knowledge, even though the model had been given sufficient attentions for around two decades, no numerical schemes for solving the B-SPF model can be announced to possess the following three properties, namely, linear, decoupled, and unconditionally energy stable. Here the term "unconditionally" means the scheme is energy stable at the discrete level irrespectively of the coarseness of the temporal or spatial discretizations. Actually, even for the partial model without flow, there still exist several challenging issues for algorithm developments, including the proper discretization for the anisotropic coefficient, the stiffness issue induced by the nonlinear double-well potential, and the nonlinear coupling between the phase variable and latent heat. Some attempts had been made in this direction, however, most of the available schemes are either nonlinear which need some efficient iterative solvers, and/or do not preserve energy stability at all, cf. [3,28,34,35,38,41, 42]. In [64], for the partial model, the authors applied the Invariant Energy Quadratization (IEQ) approach to develop a second-order, energy stable scheme by enforcing the free-energy density as an invariant, quadratic functional in terms of new, auxiliary variables and treating the nonlinear terms semi-explicitly. However, the energy stability preserves only when the temperature is a constant. Meanwhile, even though the scheme follows the discrete energy law formally, it is quite challenging to show the discrete energy obtained in [64] is bounded from below rigorously.

Compared with the partial model without flow, in addition to those numerical challenges mentioned above, the B-SPF flow coupled model is conceivably more complicated for algorithms design since we have to develop efficient temporal discretizations for the nonlinear coupling terms among the velocity field, temperature, pressure, and the weight factor which appears almost everywhere in the momentum equation and the continuity equation. Thus the main objective of this paper is to develop a time marching scheme that is not only easy-to-implement (linear and decoupled) but also unconditionally energy stable for solving the B-SPF flow coupled model. We first reformulate the model into a form which is suitable for numerical approximations and establish its energy law. Then, we develop the scheme by combining several effective approaches, including, (i) the *IEQ approach with linear stabilizers* (Stabilized-IEQ method) to discretize the anisotropic potential; (ii) the *modified projection method* to decouple the pressure from the velocity; and (iii) some subtle *implicit-explicit* treatments to discretize the weight factor and nonlinear convections. We rigorously prove that the developed scheme is unconditionally energy stable. To the best of the author's knowledge, for the flow coupled anisotropic solidification system, this is the first scheme with provable unconditional energy stabilities.

The rest of the paper is organized as follows. In Section 2, we describe the B-SPF flow coupled model and establish its energy law for the slightly modified version. In Section 3, we construct a linear, decoupled, energy stable numerical scheme for solving the coupled nonlinear system. In Section 4, we present a number of numerical results to illustrate the efficiency of the proposed scheme. Some concluding remarks are given in Section 5.

2. The model equation and its energy law

Now we give a brief description for the anisotropic phase field solidification model with melt convection in the liquid phase. Let Ω be a smooth, open, bounded, connected domain in $\mathbb{R}^d$ with $d = 2, 3$, we introduce a scalar function $\phi(\boldsymbol{x}, t)$ which is an order parameter to label the liquid and solid phase, where $\phi = 1$ for the solid and $\phi = -1$ for the liquid. These two values are connected by a smooth transitional layer with the thickness ϵ. We consider the total free energy as follows,

$$E(\phi, T) = \int_\Omega \left(\frac{1}{2} |\kappa(\nabla\phi)\nabla\phi|^2 + \frac{F(\phi)}{4\epsilon^2} + \frac{\lambda}{2\epsilon K} T^2 \right) d\boldsymbol{x}, \tag{2.1}$$

in which, ϵ is the interfacial width parameter, λ is the linear kinetic coefficient, and K is the latent heat fusion parameter that controls the speed of heat transfer along the interface, $T(\boldsymbol{x}, t)$ is the scaled temperature, $F(\phi) = (\phi^2 - 1)^2$ is the double well potential, $\kappa(\nabla\phi)$ is a function describing the anisotropic property that depends on the direction of the outer normal vector $\boldsymbol{n}$ which is the interface normal defined as $\boldsymbol{n} = -\frac{\nabla\phi}{|\nabla\phi|}$. For the 2D system, the anisotropy coefficient $\kappa(\nabla\phi)$ is usually given by

$$\kappa(\nabla\phi) = 1 + \epsilon_4\cos(m\Theta), \tag{2.2}$$

where m is the number of folds of anisotropy, ϵ_4 is the parameter for the anisotropy strength, and $\Theta = \arctan(\frac{\phi_y}{\phi_x})$, when $m = 4$ (i.e., fourfold anisotropy), for instance, $\kappa(\nabla\phi)$ can be easily reformulated in terms of the phase field variable ϕ, namely, for 2D,

$$\kappa(\nabla\phi) = (1 - 3\epsilon_4)\Big(1 + \frac{4\epsilon_4}{1 - 3\epsilon_4}\frac{\phi_x^4 + \phi_y^4}{|\nabla\phi|^4}\Big); \tag{2.3}$$

and for 3D,

$$\kappa(\nabla\phi) = (1 - 3\epsilon_4)\Big(1 + \frac{4\epsilon_4}{1 - 3\epsilon_4}\frac{\phi_x^4 + \phi_y^4 + \phi_z^4}{|\nabla\phi|^4}\Big). \tag{2.4}$$

By adopting the Allen-Cahn type (L^2-gradient flow) relaxation dynamics for the dendritic crystal growth, one obtains the governing dynamical equations via the variational approach, which reads as follows:

$$
\begin{aligned}
\tau(\phi)\phi_t &= -\frac{\delta E}{\delta\phi} - \frac{\lambda}{\epsilon}r'(\phi)T, \\
&= \nabla\cdot(\kappa^2(\nabla\phi)\nabla\phi + \kappa(\nabla\phi)|\nabla\phi|^2\boldsymbol{H}(\phi)) - \frac{f(\phi)}{\epsilon^2} - \frac{\lambda}{\epsilon}r'(\phi)T,
\end{aligned}
\tag{2.5}
$$

where $f(\phi) = F'(\phi)$, and $\boldsymbol{H}(\phi)$ is the variational derivative of $\kappa(\nabla\phi)$. In 2D, $\boldsymbol{H}(\phi)$ reads as

$$\boldsymbol{H}(\phi) = \frac{\delta\kappa(\nabla\phi)}{\delta\phi} = 4\varepsilon_4\frac{4}{|\nabla\phi|^6}\Big(\phi_x(\phi_x^2\phi_y^2 - \phi_y^4),\ \phi_y(\phi_x^2\phi_y^2 - \phi_x^4)\Big), \tag{2.6}$$

whereas in 3D, $\boldsymbol{H}(\phi)$ reads as

$$
\begin{aligned}
\boldsymbol{H}(\phi) = \frac{\delta\kappa(\nabla\phi)}{\delta\phi} = 4\varepsilon_4\frac{4}{|\nabla\phi|^6}\Big(&\phi_x(\phi_x^2\phi_y^2 + \phi_x^2\phi_z^2 - \phi_y^4 - \phi_z^4), \\
&\phi_y(\phi_y^2\phi_z^2 + \phi_x^2\phi_y^2 - \phi_x^4 - \phi_z^4),\ \phi_z(\phi_x^2\phi_z^2 + \phi_y^2\phi_z^2 - \phi_x^4 - \phi_y^4)\Big).
\end{aligned}
\tag{2.7}
$$

In (2.5), $\tau(\phi) > 0$ is the mobility constant that is chosen either as a constant [31,51], or as a function of ϕ [31], $\frac{\delta E}{\delta\phi}$ is the variational derivative of the total energy with respect to ϕ. The function $r(\phi)$, that accounts for the generation of latent heat which is only exchanged on the interface, is a phenomenological functional taking the form preserving the minima of ϕ at ± 1 independently of the local value of T. For $r(\phi)$, there are two common choices: $r(\phi) = \frac{1}{5}\phi^5 - \frac{2}{3}\phi^3 + \phi$ with $r'(\phi) = (1 - \phi^2)^2$ (cf. [31,32]); or $r(\phi) = \phi - \frac{1}{3}\phi^3$ with $r'(\phi) = 1 - \phi^2$ (cf. [2,50]).

The solidification system is composed by the liquid and solid phase, thus the fluid momentum equation vanishes in the solid phase. The confinement of the fluid velocity can be realized by a weight factor $\frac{1-\phi}{2}$, that represents the volume fraction of the liquid region, and will vanish in the solid region ($\phi = 1$). By using this weight factor, the Navier-stokes equations turn to a weighted form that reads as follows,

$$\frac{1-\phi}{2}\Big(\frac{1-\phi}{2}\boldsymbol{u}\Big)_t + \frac{1-\phi}{2}\boldsymbol{u}\cdot\nabla\boldsymbol{u} - \nu\nabla\cdot(\frac{1-\phi}{2}\nabla\boldsymbol{u}) + \frac{1-\phi}{2}\nabla p = -\nu hq(\phi)\boldsymbol{u}, \tag{2.8}$$

$$\nabla\cdot(\frac{1-\phi}{2}\boldsymbol{u}) = 0, \tag{2.9}$$

where $\boldsymbol{u}$ is the averaged fluid velocity with $\boldsymbol{u} = (u, v)$ for 2D case, p is the pressure, ν is the kinematic viscosity, h is the scaled characteristic interface width, and $q(\phi) = (1 - \phi^2)(1 + \phi)$. The last term on the right hand side of (2.8) accounts for the dissipative viscous stress in the liquid due to interactions with the solid in the diffuse interface region. It serves as a distributed momentum sink in the diffuse interface region that forces the liquid velocity to zero as $\phi \to 1$ and vanishes in the bulk liquid $\phi = -1$, cf. [2,48].

The energy equation in terms of the scaled temperature T reads as follows,

$$T_t + (\frac{1-\phi}{2}\boldsymbol{u})\cdot\nabla T = D\Delta T + Kr'(\phi)\phi_t, \tag{2.10}$$

where D is the diffusion rate of the temperature.

Without the loss of generality, we adopt the following easy boundary conditions to remove all complexities associated with the boundary integrals in this study, i.e.,

$$\partial_{\boldsymbol{n}}\phi|_{\partial\Omega} = \partial_{\boldsymbol{n}}T|_{\partial\Omega} = 0,\ \boldsymbol{u}|_{\partial\Omega} = \boldsymbol{0}, \tag{2.11}$$

where $\boldsymbol{n}$ is the outward normal of the computational domain Ω, or we can assume all variables are periodic.

The model equations (2.5)-(2.8)-(2.9)-(2.10)-(2.11) follows the dissipative energy law. By taking the L^2 inner product of (2.5) with ϕ_t, of (2.8) with $\mathbf{u}$ and using (2.9), of (2.10) with $\frac{\lambda}{\epsilon K}T$, using the integration by parts, and combining the obtained equalities, we obtain the following energy law

$$\frac{d}{dt}E_{tot}(\phi, T, \mathbf{u}) = -\|\sqrt{\tau(\phi)}\phi_t\|^2 - \frac{\lambda D}{\epsilon K}\|\nabla T\|^2 - \nu(\frac{1-\phi}{2}\nabla\mathbf{u}, \nabla\mathbf{u}) - \nu h(q(\phi)\mathbf{u}, \mathbf{u}), \tag{2.12}$$

where

$$E_{tot}(\phi, T, \mathbf{u}) = \int_\Omega \left(\frac{1}{2}|\kappa(\nabla\phi)\nabla\phi|^2 + \frac{F(\phi)}{4\epsilon^2} + \frac{\lambda}{2\epsilon K}T^2 + \frac{1}{2}\left(\frac{1-\phi}{2}\mathbf{u}\right)^2\right)d\boldsymbol{x}. \tag{2.13}$$

Remark 2.1. It is remarkable that, the momentum equation that was given in Beckerman's model [2] reads as

$$\left(\frac{1-\phi}{2}\mathbf{u}\right)_t + \frac{1-\phi}{2}\mathbf{u}\cdot\nabla\mathbf{u} - \nu\Delta(\frac{1-\phi}{2}\mathbf{u}) + \frac{1-\phi}{2}\nabla p = -\nu hq(\phi)\mathbf{u}. \tag{2.14}$$

However, if the momentum equation is formatted as (2.14), then the energy dissipation law does not hold at all which can be justified by taking the L^2 inner product of (2.14) with $\mathbf{u}$. Therefore, we slightly modify (2.14) into (2.8) by replacing the time derivative term $(\frac{1-\phi}{2}\mathbf{u})_t$ by $\frac{1-\phi}{2}(\frac{1-\phi}{2}\mathbf{u})_t$, and the diffusion term $\Delta(\frac{1-\phi}{2}\mathbf{u})$ by $\nabla\cdot(\frac{1-\phi}{2}\nabla\mathbf{u})$. Through this slight modification, the new momentum equation (2.8) is not only consistent to (2.14) for the solid phase ($\phi = 1$) and liquid phase ($\phi = -1$), but also can be shown to follow the energy dissipation law.

Remark 2.2. Note that the last two terms on the right hand side of (2.12) could be non-negative, which implies the total energy might not be dissipative. The signs of these two terms are determined by the value of weight factor $\frac{1-\phi}{2}$. This energy law is "physically" reasonable since the value of ϕ is expected to be situated in $[-1, 1]$ in the ideal situation. But mathematically, for the PDE system, it is quite challenging to show whether there exists a unique solution and whether the solution follows the maximum principle. Likewise, it is also challenging to develop schemes which can ensure the range of numerical solution of ϕ to be in $[-1, 1]$ (discrete maximum principle). To fix the problem of non-dissipative energy, in next section, we simply replace the ϕ using its clamped value in $[-1, 1]$ as defined in (3.8).

Remark 2.3. Note in many previous works, the choice of the function $r'(\phi)$ in (2.5) and that in (2.10) are not consistent. For instance, $r'(\phi)$ in (2.5) is set to be $(1-\phi^2)^2$ or $1-\phi^2$, but $r'(\phi)$ in (2.10) is set to be 1 instead, cf. [31]. At this time, the resultant PDE system for (ϕ, T) can not preserve the energy dissipation law any more, see the detailed discussions in [31].

3. Numerical schemes

Now we aim to develop efficient schemes for solving the flow coupled solidification dendritic model (2.5)-(2.8)-(2.9)-(2.10)-(2.11), in which the main challenging issues are to find proper approaches to discretize numerous nonlinear terms, particularly, (i) the coupling between the pressure and the velocity through the weighted continuity equation (2.9); (ii) the cubic term $f(\phi)$ in (2.5); (iii) the second order terms associated with the anisotropic gradient-dependent coefficient $\kappa(\nabla\phi)$; (iv) the term coupling the phase field variable and temperature in (2.5) and (2.10); (v) the nonlinear convective term in (2.10); and (vi) the coupling among the weight factor $\frac{1-\phi}{2}$, the velocity, and the pressure.

If the weight factor is a constant, the first difficulty (i) actually has been well studied during the last forty years; e.g., projection-type methods are one of the best options to solve it (cf. the review in [18] and the references therein). However, the momentum equation (2.8) and the associated divergence free condition (2.9) become very unusual due to the weight factor appearing almost everywhere. Thus the projection-type methods must be modified accordingly.

For the second difficulty (ii), we recall that there have been several established numerical techniques that can preserve the unconditional energy stability for phase field models, for instances, the convex splitting approach [11,21,54], the linear stabilized-explicit approach [14,23,24,44–46,52,55], the mixed variational methods [16,17,37], the IEQ approach [4,56,58,59, 62–64], and a variety of other methods [9,19,26], etc. However, the convex splitting and stabilized-explicit approaches might not be suitable choices for solving this model since it is not clear how the anisotropic gradient potential could be split into the combinations of the convex and concave parts for the former method, and it is quite challenging to prove the energy stability for the latter method.

Nonetheless, we choose the recently developed IEQ approach to discretize the cubic polynomial term $f(\phi)$, and the second order term with the anisotropic coefficient $\kappa(\nabla\phi)$. Since the second order term is treated in the semi-implicit way, we add two extra linear stabilizing terms to enhance the stability. These two terms are also crucial to prove the well-posedness of the obtained linear system, see the detailed proof of Theorem 3.1.

The key procedure of the IEQ approach is to make the free energy potential to be quadratic via one or more auxiliary variables. Thus we define an auxiliary variable as follows:

$$U = \sqrt{\frac{1}{2}|\kappa(\nabla\phi)\nabla\phi|^2 + \frac{1}{4\epsilon^2}F(\phi) + B}, \tag{3.1}$$

where B is a constant that can ensure the radicand positive (in all numerical examples, we let $B \sim O(10^4)$ which is the same order of $\frac{1}{\epsilon^2}$). Thus the total free energy (2.13) can be rewritten as

$$E(\phi, U, T, \mathbf{u}) = \int_\Omega (U^2 + \frac{\lambda}{2\epsilon K} T^2 + \frac{1}{2}\left(\frac{1-\phi}{2}\mathbf{u}\right)^2 - B)d\mathbf{x}. \tag{3.2}$$

By taking the time derivative of the new variable U, we then reformulate the system (2.5)-(2.8)-(2.9)-(2.10)-(2.11) as the following equivalent PDE system,

$$\tau(\phi)\phi_t = -Z(\phi)U - \frac{\lambda}{\epsilon}r'(\phi)T, \tag{3.3}$$

$$U_t = \frac{1}{2}Z(\phi)\phi_t, \tag{3.4}$$

$$T_t + (\frac{1-\phi}{2}\mathbf{u}) \cdot \nabla T = D\Delta T + Kr'(\phi)\phi_t, \tag{3.5}$$

$$\frac{1-\phi}{2}\left(\frac{1-\phi}{2}\mathbf{u}\right)_t + \frac{1-\phi}{2}\mathbf{u} \cdot \nabla\mathbf{u} - \nu\nabla\cdot(\frac{1-\hat\phi}{2}\nabla\mathbf{u}) + \frac{1-\phi}{2}\nabla p = -\nu h q(\hat\phi)\mathbf{u}, \tag{3.6}$$

$$\nabla\cdot(\frac{1-\phi}{2}\mathbf{u}) = 0, \tag{3.7}$$

where

$$\hat\phi = \begin{cases} 1, & \phi \in (1,\infty), \\ \phi, & \phi \in [-1,1], \\ -1, & \phi \in (-\infty,-1), \end{cases} \tag{3.8}$$

$$Z(\phi) = \frac{-\nabla\cdot(\kappa^2(\nabla\phi)\nabla\phi + \kappa(\nabla\phi)|\nabla\phi|^2\boldsymbol{H}(\phi)) + \frac{1}{\epsilon^2}f(\phi)}{\sqrt{\frac{1}{2}|\kappa(\nabla\phi)\nabla\phi|^2 + \frac{1}{4\epsilon^2}F(\phi) + B}}. \tag{3.9}$$

The initial conditions are given by

$$\begin{cases} \phi(t=0) = \phi_0, \ T(t=0) = T_0, \\ U(t=0) = \sqrt{\frac{1}{2}|\kappa(\nabla\phi_0)\nabla\phi_0|^2 + \frac{1}{4\epsilon^2}F(\phi_0) + B}, \\ \mathbf{u}(t=0) = \mathbf{u}_0, \ p(t=0) = p_0. \end{cases} \tag{3.10}$$

The boundary conditions are still (2.11) that we alluded before.

This new and equivalent system (3.3)-(3.7) also follows an energy dissipative law. By taking the L^2 inner product of (3.3) with ϕ_t, of (3.4) with $-2U$, of (3.5) with $\frac{\lambda}{\epsilon K}T$, of (3.6) with $\mathbf{u}$ and using (3.7), performing integration by parts, and summing up all equalities, we can obtain the energy dissipation law of the new system (3.3)-(3.7) as

$$\frac{d}{dt}E(\phi, U, T, \mathbf{u}) = -\|\sqrt{\tau(\phi)}\phi_t\|^2 - \frac{\lambda D}{\epsilon K}\|\nabla T\|^2 - \nu\|\sqrt{\left|\frac{1-\phi}{2}\right|}\nabla\mathbf{u}\|^2 - \nu h\|\sqrt{|q(\phi)|}\mathbf{u}\|^2. \tag{3.11}$$

Next we will develop time marching algorithms for solving the transformed system (3.3)-(3.5). The proposed schemes should formally follow the new energy dissipation law (3.11) in the discrete sense, instead of the energy law for the originated system (2.12). It can be shown that the discrete transformed energy is the approximation to the original energy with the first-order accuracy, which is verified by the rigorous error estimates and numerical simulations in [61].

Let $\delta t > 0$ be a time step size and set $t^n = n\delta t$ for $0 \le n \le N$ with $T = N\delta t$. We also denote the L^2 inner product of any two spatial functions $\varphi_1(\mathbf{x})$ and $\varphi_2(\mathbf{x})$ by $(\varphi_1(\mathbf{x}), \varphi_2(\mathbf{x})) = \int_\Omega \varphi_1(\mathbf{x})\varphi_2(\mathbf{x})d\mathbf{x}$, and the L^2 norm of the function $\varphi(\mathbf{x})$ by $\|\varphi\|^2 = (\varphi, \varphi)$. Let φ^n denote the numerical approximation to $\varphi(\cdot, t)|_{t=t^n}$ for any function φ.

We construct a first-order time marching scheme for solving the system (3.3)-(3.7), as follows.

Assuming ϕ^n, T^n, U^n, $(\psi\mathbf{u})^n$, p^n are known, we update ϕ^{n+1}, T^{n+1}, U^{n+1}, $\tilde{\mathbf{u}}^{n+1}$, $(\psi\mathbf{u})^{n+1}$, p^{n+1} by solving the following three steps:

Step 1:

$$\tau(\phi^n)\frac{\phi^{n+1} - \phi^n}{\delta t} + \frac{S_1}{\epsilon^2}(\phi^{n+1} - \phi^n) - S_2\Delta(\phi^{n+1} - \phi^n) = -Z^n U^{n+1} - \frac{\lambda}{\epsilon}r'(\phi^n)T^{n+1}, \tag{3.12}$$

$$U^{n+1} - U^n = \frac{1}{2}Z^n(\phi^{n+1} - \phi^n), \tag{3.13}$$

$$\frac{T^{n+1} - T^n}{\delta t} + (\psi^n \mathbf{u}^n) \cdot \nabla T^{n+1} - D \Delta T^{n+1} = K r'(\phi^n) \frac{\phi^{n+1} - \phi^n}{\delta t}, \tag{3.14}$$

$$\partial_{\mathbf{n}} \phi^{n+1}|_{\partial \Omega} = \partial_{\mathbf{n}} T^{n+1}|_{\partial \Omega} = 0, \tag{3.15}$$

where

$$\psi^n = \frac{1 - \phi^n}{2}, \ Z^n = Z(\phi^n), \tag{3.16}$$

and S_i with $i = 1, 2$ are two positive stabilizing parameters;

Step 2:

$$\psi^{n+1} \frac{\psi^{n+1} \widetilde{\mathbf{u}}^{n+1} - \psi^n \mathbf{u}^n}{\delta t} + \psi^n \mathbf{u}^n \cdot \nabla \widetilde{\mathbf{u}}^{n+1} - \nu \nabla \cdot (\hat{\psi}^{n+1} \nabla \widetilde{\mathbf{u}}^{n+1}) \tag{3.17}$$

$$+ \psi^{n+1} \nabla p^n = -\nu h q(\hat{\phi}^{n+1}) \widetilde{\mathbf{u}}^{n+1},$$

$$\widetilde{\mathbf{u}}^{n+1}|_{\partial \Omega} = 0; \tag{3.18}$$

where $\hat{\psi}^n = \frac{1 - \hat{\phi}^n}{2}$;

Step 3:

$$\frac{\psi^{n+1} \mathbf{u}^{n+1} - \psi^{n+1} \widetilde{\mathbf{u}}^{n+1}}{\delta t} + \nabla(p^{n+1} - p^n) = 0, \tag{3.19}$$

$$\nabla \cdot (\psi^{n+1} \mathbf{u}^{n+1}) = 0, \tag{3.20}$$

$$(\psi^{n+1} \mathbf{u}^{n+1}) \cdot \mathbf{n}|_{\partial \Omega} = 0. \tag{3.21}$$

Remark 3.1. Two first-order linear stabilizers (associated with S_1 and S_2) are added in the scheme (3.12) to enhance the stability since anisotropic coefficient $\kappa(\nabla \phi)$ is treated semi-implicitly which can cause large spatial oscillations and lead to blow up for large time steps, see [57]. These stabilizers are two commonly used linear stabilizers in the stabilized-explicit method for solving the isotropic or anisotropic phase field model, cf. [45,46,52,57]. The errors that these two terms introduce are of order $S_1 \delta t \phi(\cdot)$ and $S_2 \delta t \Delta \phi(\cdot)$, respectively, which are of the same order as the error introduced by the first-order extrapolation of the nonlinear term $f(\phi)$ and the Laplacian term $\Delta \phi$. Therefore, the magnitude of S_1 and S_2 should be comparable with $|f(\phi^n)|_\infty$ and $|\kappa(\nabla \phi^n)|_\infty$. In our numerical simulations, we use $S_1 = S_2 = 4$ which appears to provide a good balance between stability and accuracy.

Remark 3.2. For step 3, by applying the divergence operator $\nabla \cdot$ and using (3.20), we can obtain the following Poisson equation for p^{n+1} with the homogeneous Neumann boundary conditions,

$$\begin{cases} -\Delta(p^{n+1} - p^n) = -\frac{1}{\delta t} \nabla \cdot (\psi^{n+1} \widetilde{\mathbf{u}}^{n+1}), \\ \partial_{\mathbf{n}} p^{n+1}|_{\partial \Omega} = 0. \end{cases} \tag{3.22}$$

Once $p^{n+1} - p^n$ is computed from (3.22), we update $\psi^{n+1} \mathbf{u}^{n+1}$ by using (3.19), i.e.,

$$\psi^{n+1} \mathbf{u}^{n+1} = \psi^{n+1} \widetilde{\mathbf{u}}^{n+1} - \delta t \nabla(p^{n+1} - p^n). \tag{3.23}$$

It is remarkable that the computations will overflow if we try to obtain $\mathbf{u}^{n+1}$ by dividing ψ^{n+1} for both sides of (3.23), since ψ^{n+1} may equal to zero at plenty of grid points. But fortunately, we only need the values of $\psi^n \mathbf{u}^n$ instead of $\mathbf{u}^n$ to obtain $\widetilde{\mathbf{u}}^{n+1}$ in the momentum equation (3.17). Therefore, in practice, the algorithm will not blow up and we only need to store the values of $\psi^n \mathbf{u}^n$ at each time step.

Remark 3.3. The computations of $(\phi, T)^{n+1}$, $\widetilde{\mathbf{u}}^{n+1}$, and p^{n+1} are totally decoupled via a first-order pressure-correction scheme [18] with some modifications. Furthermore, through some subtle implicit-explicit discretizations for the stress and convective terms, the above scheme is totally linear thus it is very easy-to-implement.

In step 1, the new auxiliary variable U and the two added linear stabilizers will not result in extra computational cost since we can implement the scheme by the following procedure. We rewrite (3.13) as follows,

$$U^{n+1} = \frac{1}{2} Z^n \phi^{n+1} + A_1, \tag{3.24}$$

with $A_1 = U^n - \frac{1}{2} Z^n \phi^n$ and substitute (3.24) to (3.12), then the system (3.12)-(3.14) can be rewritten as

$$Q\left(\phi^{n+1}\right) + \frac{\lambda}{\epsilon} r'(\phi^n) T^{n+1} = f_1, \tag{3.25}$$

$$\frac{\lambda}{\epsilon K} T^{n+1} + \delta t \frac{\lambda}{\epsilon K} (\psi^n \mathbf{u}^n) \cdot \nabla T^{n+1} - \delta t \frac{\lambda D}{\epsilon K} \Delta T^{n+1} - \frac{\lambda}{\epsilon} r'(\phi^n) \phi^{n+1} = f_2, \tag{3.26}$$

where

$$Q\left(\phi^{n+1}\right) = \frac{1}{\delta t} \tau(\phi^n) \phi^{n+1} + \frac{S_1}{\epsilon^2} \phi^{n+1} - S_2 \Delta \phi^{n+1} + \frac{1}{2} Z^n Z^n \phi^{n+1}, \tag{3.27}$$

and f_1, f_2 include only terms from previous time steps. In practice, we solve (3.25)-(3.26) directly to obtain ϕ^{n+1} and T^{n+1}, and then update the new variable U^{n+1} from (3.24).

Furthermore, we notice $(Q(\phi), \psi) = (\phi, Q(\psi))$ when ϕ, ψ satisfy the boundary conditions in (2.11), that means the linear operator $Q(\phi)$ is self-adjoint; and $(Q(\phi), \phi) \geq 0$, where "=" is valid if and only if $\phi \equiv 0$, that means the linear operator $Q(\phi)$ is actually symmetric positive definite.

We now show the well-posedness of the weak form of the above linear system (3.25)-(3.26). For the wellposedness of projection type scheme (3.17)-(3.19), we omit the proof since it is similar. In the following arguments, we will only consider the boundary condition (2.11) for convenience. For the case of periodic boundary conditions, the proof is similar.

The weak form of (3.25)-(3.26) can be written as the following system with the unknowns $(\phi, T) \in (H^1, H^1)(\Omega)$,

$$\frac{1}{\delta t}(\tau(\phi^n)\phi, \varphi) + \frac{S_1}{\epsilon^2}(\phi, \varphi) + S_2(\nabla\phi, \nabla\varphi) + \frac{1}{2}(Z^n\phi, Z^n\varphi) + \frac{\lambda}{\epsilon}(r'(\phi^n)T, \varphi) = (f_1, \varphi), \tag{3.28}$$

$$\frac{\lambda}{\epsilon K}(T, \vartheta) + \delta t \frac{\lambda}{\epsilon K}((\psi^n\mathbf{u}^n) \cdot \nabla T, \vartheta) + \delta t \frac{\lambda D}{\epsilon K}(\nabla T, \nabla\vartheta) - \frac{\lambda}{\epsilon}(r'(\phi^n)\phi, \vartheta) = (f_2, \vartheta), \tag{3.29}$$

for any $(\varphi, \vartheta) \in (H^1, H^1)(\Omega)$.

We denote the above bilinear system (3.28)-(3.29) as the bilinear system

$$(\boldsymbol{A}(\boldsymbol{X}), \boldsymbol{Y}) = (\boldsymbol{B}, \boldsymbol{Y}), \tag{3.30}$$

where $\boldsymbol{A}$ is the linear operator, $\boldsymbol{X} = (\phi, T)^T$, $\boldsymbol{Y} = (\varphi, \vartheta)^T$, and $\boldsymbol{X}, \boldsymbol{Y} \in (H^1, H^1)(\Omega)$.

Theorem 3.1. *The bilinear system* (3.30) *admits a unique solution* $(\phi, T) \in (H^1, H^1)(\Omega)$.

Proof. (i) For any $\boldsymbol{X} = (\phi, T)^T$ and $\boldsymbol{Y} = (\varphi, \vartheta)^T$ with $\boldsymbol{X}, \boldsymbol{Y} \in (H^1, H^1)(\Omega)$, we have

$$(\boldsymbol{A}(\boldsymbol{X},)\boldsymbol{Y}) \leq C_1(\|\phi\|_{H^1} + \|T\|_{H^1})(\|\varphi\|_{H^1} + \|\vartheta\|_{H^1}), \tag{3.31}$$

where C_1 is a constant depending on δt, S_1, S_2, λ, ϵ, D, K, $\|Z^n\|_\infty$, $\|\psi^n\mathbf{u}^n\|_\infty$, and $\|r'(\phi^n)\|_\infty$. Therefore, the bilinear system $(\boldsymbol{A}(\boldsymbol{X}), \boldsymbol{Y})$ is bounded.

(ii) It is easy to derive that

$$\begin{aligned}
(\boldsymbol{A}(\boldsymbol{X}), \boldsymbol{X}) &= \frac{1}{\delta t}\|\sqrt{\tau(\phi^n)}\phi\|^2 + \frac{S_1}{\epsilon^2}\|\phi\|^2 + S_2\|\nabla\phi\|^2 \\
&\quad + \frac{1}{2}\|Z^n\phi\|^2 + \frac{\lambda}{\epsilon K}\|T\|^2 + \delta t\frac{\lambda D}{\epsilon K}\|\nabla T\|^2 \\
&\geq C_2(\|\phi\|_{H^1}^2 + \|T\|_{H^1}^2),
\end{aligned} \tag{3.32}$$

where C_2 is a constant depending on δt, S_1, S_2, ϵ, λ, D, K. Thus the bilinear system $(\boldsymbol{A}(\boldsymbol{X}), \boldsymbol{Y})$ is coercive.

Then from the Lax-Milgram theorem, we conclude the linear system (3.30) admits a unique solution $(\phi, T) \in (H^1, H^1)(\Omega)$. $\quad\square$

Remark 3.4. The stabilizer S_2 is crucial to ensure the coercivity of the bilinear system in $H^1(\Omega)$. If we set $S_2 = 0$, then we can only show that the system admits a unique solution ϕ in $L^2(\Omega)$ that might bring up some essential difficulties for error estimates. However, to implement the error analysis for the scheme is absolutely non-trivial due to the nonlinear anisotropic terms and weight factor. We will consider the subsequent error analysis in our future work by following the same lines as the analytical work for isotropic Allen-Cahn/Cahn-Hilliard models in [61]. The error estimates for the fully discrete schemes in the context of finite element method or spectral method, we refer to [12,14,45].

Now we prove the scheme (3.12)-(3.21) is unconditionally energy stable.

Theorem 3.2. *The scheme* (3.12)-(3.21) *is unconditionally energy stable which satisfies the following discrete energy dissipation law,*

$$
\begin{aligned}
E^{n+1} \leq E^n - \delta t \|\sqrt{\tau(\phi^n)}\frac{\phi^{n+1}-\phi^n}{\delta t}\|^2 - \delta t\frac{\lambda D}{\epsilon K}\|\nabla T^{n+1}\|^2 \\
- \nu h \delta t \|\sqrt{q(\hat{\phi}^n)}\widetilde{\mathbf{u}}^{n+1}\|^2 - \nu \delta t\|\sqrt{\hat{\psi}^{n+1}}\nabla\widetilde{\mathbf{u}}^{n+1}\|^2,
\end{aligned}
\tag{3.33}
$$

where

$$
E^{n+1} = \|U^{n+1}\|^2 + \frac{\lambda}{2\epsilon K}\|T^{n+1}\|^2 + \frac{1}{2}\|\psi^{n+1}\mathbf{u}^{n+1}\|^2 + \frac{\delta t^2}{2}\|\nabla p^{n+1}\|^2.
\tag{3.34}
$$

Proof. By taking the L^2 inner product of (3.12) with $\phi^{n+1} - \phi^n$ and using integration by parts, we obtain

$$
\begin{aligned}
\delta t\|\sqrt{\tau(\phi^n)}\frac{\phi^{n+1}-\phi^n}{\delta t}\|^2 + \delta t^2\frac{S_1}{\epsilon^2}\|\frac{\phi^{n+1}-\phi^n}{\delta t}\|^2 + S_2\delta t^2\|\frac{\nabla(\phi^{n+1}-\phi^n)}{\delta t}\|^2 \\
= -(Z^n U^{n+1}, \phi^{n+1}-\phi^n) - \frac{\lambda}{\epsilon}(r'(\phi^n)T^{n+1}, \phi^{n+1}-\phi^n).
\end{aligned}
\tag{3.35}
$$

By taking the L^2 inner product of (3.13) with $2U^{n+1}$ and using the following identity

$$
2a(a-b) = a^2 - b^2 + (a-b)^2,
\tag{3.36}
$$

we obtain

$$
\|U^{n+1}\|^2 - \|U^n\|^2 + \|U^{n+1} - U^n\|^2 = (Z^n(\phi^{n+1}-\phi^n), U^{n+1}).
\tag{3.37}
$$

By taking the L^2 inner product of (3.14) with $\delta t\frac{\lambda}{\epsilon K}T^{n+1}$, and using (3.36), we obtain

$$
\begin{aligned}
\frac{\lambda}{2\epsilon K}(\|T^{n+1}\|^2 - \|T^n\|^2 + \|T^{n+1} - T^n\|^2) + \frac{\lambda D}{\epsilon K}\delta t\|\nabla T^{n+1}\|^2 \\
= \frac{\lambda}{\epsilon}(r'(\phi^n)(\phi^{n+1}-\phi^n), T^{n+1}),
\end{aligned}
\tag{3.38}
$$

where the convective term vanishes since the following equality holds

$$
\int_\Omega (\psi^n\mathbf{u}^n \cdot \nabla)T^{n+1}T^{n+1}dx = 0,
\tag{3.39}
$$

if $(\psi^n\mathbf{u}^n) \cdot \mathbf{n}|_{\partial\Omega} = 0$ and $\nabla\cdot(\psi^n\mathbf{u}^n) = 0$.

By combining (3.35), (3.37), and (3.38), we obtain

$$
\begin{aligned}
\delta t\|\sqrt{\tau(\phi^n)}\frac{\phi^{n+1}-\phi^n}{\delta t}\|^2 + \delta t^2\frac{S_1}{\epsilon^2}\|\frac{\phi^{n+1}-\phi^n}{\delta t}\|^2 + \delta t^2 S_2\|\frac{\nabla(\phi^{n+1}-\phi^n)}{\delta t}\|^2 \\
+ \|U^{n+1}\|^2 - \|U^n\|^2 + \|U^{n+1} - U^n\|^2 \\
+ \frac{\lambda}{2\epsilon K}(\|T^{n+1}\|^2 - \|T^n\|^2 + \|T^{n+1} - T^n\|^2) + \frac{\lambda D}{\epsilon K}\delta t\|\nabla T^{n+1}\|^2 = 0.
\end{aligned}
\tag{3.40}
$$

By taking the L^2 inner product of (3.17) with $\delta t\widetilde{\mathbf{u}}^{n+1}$ and using (3.36), we obtain

$$
\begin{aligned}
\frac{1}{2}\|\psi^{n+1}\widetilde{\mathbf{u}}^{n+1}\|^2 - \frac{1}{2}\|\psi^n\mathbf{u}^n\|^2 + \frac{1}{2}\|\psi^{n+1}\widetilde{\mathbf{u}}^{n+1} - \psi^n\mathbf{u}^n\|^2 \\
+ \nu\delta t\|\sqrt{|\psi^{n+1}|}\nabla\widetilde{\mathbf{u}}^{n+1}\|^2 + \delta t(\psi^{n+1}\nabla p^n, \widetilde{\mathbf{u}}^{n+1}) \\
= -\nu h\delta t\sqrt{|q(\phi^n)|}\widetilde{\mathbf{u}}^{n+1}\|^2,
\end{aligned}
\tag{3.41}
$$

where the convective term vanishes since the following equality holds

$$
\int_\Omega (\psi^n\mathbf{u}^n \cdot \nabla)\widetilde{\mathbf{u}}^{n+1} \cdot \widetilde{\mathbf{u}}^{n+1}dx = 0,
\tag{3.42}
$$

when $(\psi^n\mathbf{u}^n) \cdot \mathbf{n}|_{\partial\Omega} = 0$ and $\nabla\cdot(\psi^n\mathbf{u}^n) = 0$.

By taking the L^2 inner product of (3.19) with $\delta t\psi^{n+1}\mathbf{u}^{n+1}$, we obtain

$$
\frac{1}{2}\|\psi^{n+1}\mathbf{u}^{n+1}\|^2 - \frac{1}{2}\|\psi^{n+1}\widetilde{\mathbf{u}}^{n+1}\|^2 + \frac{1}{2}\|\psi^{n+1}\mathbf{u}^{n+1} - \psi^{n+1}\widetilde{\mathbf{u}}^{n+1}\|^2 = 0.
\tag{3.43}
$$

By taking the L^2 inner product of (3.19) with $\delta t^2 \nabla p^n$ and using (3.20), we obtain

$$\frac{\delta t^2}{2}(\|\nabla p^{n+1}\|^2 - \|\nabla p^n\|^2) - \frac{\delta t^2}{2}\|\nabla p^{n+1} - \nabla p^n\|^2 = \delta t(\psi^{n+1}\widetilde{\mathbf{u}}^{n+1}, \nabla p^n). \tag{3.44}$$

By taking the square of (3.19) and multiplying with $\frac{\delta t^2}{2}$, we obtain

$$\frac{\delta t^2}{2}\|\nabla p^{n+1} - \nabla p^n\|^2 = \frac{1}{2}\|\psi^{n+1}\mathbf{u}^{n+1} - \psi^{n+1}\widetilde{\mathbf{u}}^{n+1}\|^2. \tag{3.45}$$

By combining (3.41), (3.43), (3.44), and (3.45), we obtain

$$\begin{aligned}
&\frac{1}{2}\|\psi^{n+1}\mathbf{u}^{n+1}\|^2 - \frac{1}{2}\|\psi^n\mathbf{u}^n\|^2 + \frac{1}{2}\|\psi^{n+1}\widetilde{\mathbf{u}}^{n+1} - \psi^n\mathbf{u}^n\|^2 + \nu\delta t\|\sqrt{\hat{\psi}^{n+1}}\,\nabla\widetilde{\mathbf{u}}^{n+1}\|^2 \\
&\qquad + \frac{\delta t^2}{2}(\|\nabla p^{n+1}\|^2 - \|\nabla p^n\|^2) = -\nu h\delta t\|\sqrt{q(\hat{\phi}^n)}\,\widetilde{\mathbf{u}}^{n+1}\|^2.
\end{aligned} \tag{3.46}$$

Finally, by combining (3.40) and (3.46), we obtain

$$\begin{aligned}
&\|U^{n+1}\|^2 - \|U^n\|^2 + \|U^{n+1} - U^n\|^2 + \frac{\lambda}{2\epsilon K}(\|T^{n+1}\|^2 - \|T^n\|^2 + \|T^{n+1} - T^n\|^2) \\
&\quad + \frac{1}{2}\|\psi^{n+1}\mathbf{u}^{n+1}\|^2 - \frac{1}{2}\|\psi^n\mathbf{u}^n\|^2 + \frac{1}{2}\|\psi^{n+1}\widetilde{\mathbf{u}}^{n+1} - \psi^n\mathbf{u}^n\|^2 \\
&\quad + \frac{\delta t^2}{2}(\|\nabla p^{n+1}\|^2 - \|\nabla p^n\|^2) \\
&\quad + \delta t^2\frac{S_1}{\epsilon^2}\|\frac{\phi^{n+1} - \phi^n}{\delta t}\|^2 + \delta t^2 S_2\|\frac{\nabla(\phi^{n+1} - \phi^n)}{\delta t}\|^2 \\
&= -\nu h\delta t\|\sqrt{q(\hat{\phi}^n)}\,\widetilde{\mathbf{u}}^{n+1}\|^2 - \frac{\lambda D}{\epsilon K}\delta t\|\nabla T^{n+1}\|^2 \\
&\quad - \nu\delta t(\sqrt{\hat{\psi}^{n+1}}\,\nabla\widetilde{\mathbf{u}}^{n+1}\|^2 - \delta t\|\sqrt{\tau(\phi^n)}\frac{\phi^{n+1} - \phi^n}{\delta t}\|^2.
\end{aligned} \tag{3.47}$$

We can obtain the desired result after dropping some unnecessary positive terms. $\quad\square$

Remark 3.5. For the reduced dendritic model without flow, second order unconditional energy stable schemes had been developed in our recent work, see [57]. For the flow coupled anisotropic solidification model, however, it is absolutely non-trivial to develop second-order time marching schemes that can preserve unconditionally energy stabilities where the main difficulty lies on the treatments for weight factor $\frac{1-\phi}{2}$ in the Navier-Stokes equations. We leave this part to the future work. In addition, although we consider only time discrete schemes in this study, the results can be carried over to any consistent finite-dimensional Galerkin approximations in the space since the proofs are all based on a variational formulation with all test functions in the same space as the space of the trial functions.

4. Numerical simulations

In this section, we present various numerical examples to validate the proposed schemes and demonstrate their accuracy, energy stability and efficiency.

4.1. Brief description of the full discretization schemes

In all of the following examples, we consider a two-dimensional rectangular domain $\Omega = [0, L_1] \times [0, L_2]$. For x-axis, we set the periodic boundary conditions thus we adopt the Fourier-spectral method. For y-axis, the boundary conditions (2.11) are used and the spatial discretizations are based on the Legendre-Galerkin method [43] which results in very efficient and accurate solvers for elliptic equations with constant coefficients. We adopt the inf-sup stable (P_N, P_{N-2}) pair for the velocity and pressure, and P_N for the phase and temperature variables. For solving the coupled linear variable-coefficient system in step 1 and 2, we refer to our recent work [60] where the procedure was given in details.

4.2. Accuracy test

We first implement a numerical example with fourfold anisotropy (2.3) in 2D space to test the convergence rates of the proposed scheme. N Fourier modes are used to discretize the x-direction, and Legendre polynomials with degree up to M are used for y-direction. We set $N = 129$ and $M = 128$, so that the errors from the spatial discretization is negligible compared with the time discretization errors.
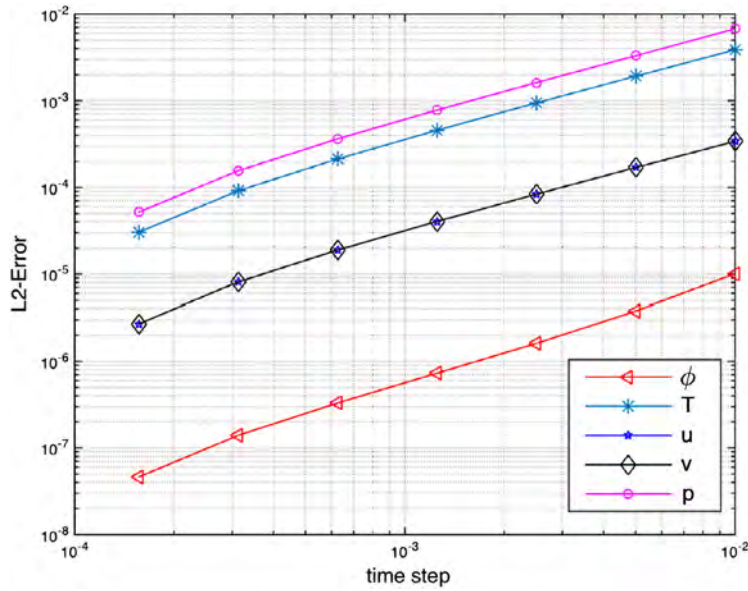
Convergence w.r.t various time steps.

Fig. 4.1. The L^2 numerical errors for all variables at $t = 0.1$, that are computed using various temporal resolutions with order parameters given in (4.1) and the initial conditions of (4.2).

The model parameters are set as follows,

$$\begin{cases} L_1 = L_2 = 3, \tau = 100, \epsilon = 0.06, \epsilon_4 = 0.05, \\ D = \lambda = K = 1, S_1 = S_2 = 4, \nu = 1, h = 0.01, B = 5 \times 10^4. \end{cases} \tag{4.1}$$

We now perform refinement tests for temporal convergence by assuming the following initial conditions

$$\begin{cases} \phi_0 = \sin(ax)\cos(by), \ T_0 = \cos(ax)\cos(by), \\ \mathbf{u}_0 = (u_0, v_0) = (0, 0.02), \ p_0 = 0, \end{cases} \tag{4.2}$$

with $a = \frac{2\pi}{L_1}$ and $b = \frac{2\pi}{L_2}$. The boundary conditions for y-direction are set as follows,

$$\begin{cases} \partial_y \phi|_{(y=0, \ y=L_2)} = 0, \ \partial_y T|_{(y=0, \ y=L_2)} = 0, \\ u|_{(y=0, \ y=L_2)} = 0, \ v|_{(y=0, \ y=L_2)} = -0.02. \end{cases} \tag{4.3}$$

Since the exact solutions are not known, we choose the solution obtained by the scheme with the time step size $\delta t = 10^{-6}$ as the benchmark solution (approximately the exact solution) for computing errors. We present the L^2 errors of each variable between the numerical solution and the exact solution at $t = 0.1$ with different time step sizes in Fig. 4.1. We observe that the scheme almost perfectly matches the first-order accuracy in time for all variables. In Fig. 4.2(b) and (c), we plot the L^2 errors of all variables at time $t = 0.1$ by refining the grid points along the x and y directions, respectively. We use a very small time step $\delta t = 10^{-6}$ so that the errors from the temporal discretization are negligible compared to the spatial discretization errors. For the x-direction, we fix the number of Legendre modes $M = 256$ and vary the number of Fourier modes N starting from 33 with an increment of 32, with a reference solution obtained using the finest resolution of $N = 257$, $M = 256$. The convergence in the y-direction is obtained in a similar way. We see that the scheme achieves the spectral accuracy in the L^2 norm.

4.3. 2D dendrite crystal growth with fourfold anisotropy

In this subsection, we investigate how the anisotropic entropy coefficient and the flow field can affect the shape of the dendritic crystal through the dynamical process in which a small crystal nucleus grows heterogeneously in 2D space. We still use the same boundary conditions specified in (4.3) but setting

$$v|_{(y=0, \ y=L_2)} = -0.008. \tag{4.4}$$

The initial conditions are set as
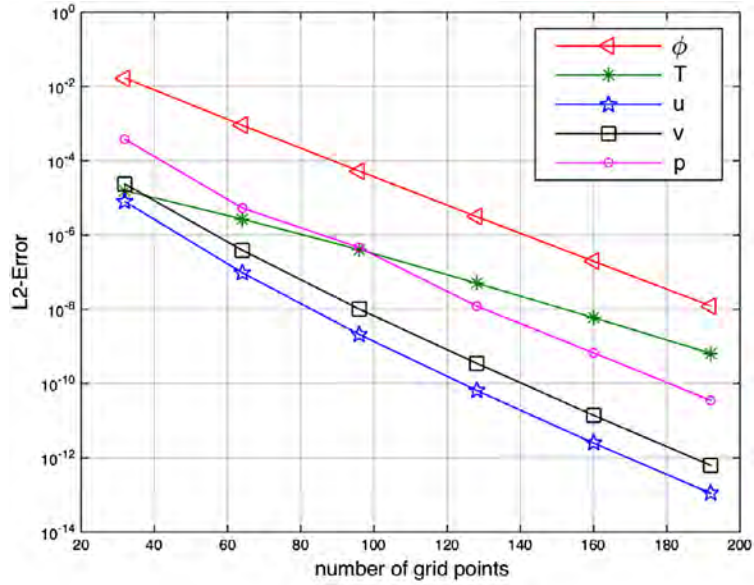
(a) Convergence w.r.t. DoFs in x-direction.
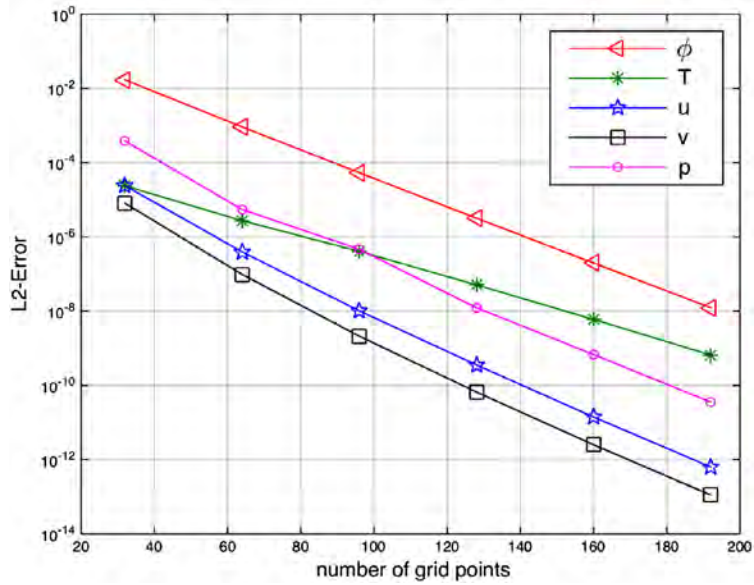
(b) Convergence w.r.t. DoFs in y-direction.

Fig. 4.2. (a) the L^2 numerical errors for all variables with respect to number of DoFs in the x direction; and (b) the L^2 numerical errors for all variables with respect to number of DoFs in the y direction. The order parameters are from (4.1) and the initial conditions are from (4.2).

$$\begin{cases} \phi_0 = \tanh(\dfrac{r_0 - \sqrt{(x - x_0)^2 + (y - y_0)^2}}{\epsilon_0}), \ T_0 = \begin{cases} 0, \ \phi > 0; \\ \hat{T}_0, \text{otherwise}; \end{cases} \\ \mathbf{u}_0 = \mathbf{0}, \ p_0 = 0, \end{cases} \tag{4.5}$$

where $x_0 = y_0 = 1.5$, $r_0 = 0.0519$, $\epsilon_0 = 0.0106$ and $\hat{T}_0 = -0.55$. The other parameters are set as follows,

$$\begin{cases} L_1 = L_2 = 3, N = 257, M = 256, \\ \tau = 4268.4, \epsilon = 0.0115, D = 0.000225, \\ K = 0.8, \lambda = 355, S_1 = S_2 = 4, \nu = 1, h = 0.01, B = 5 \times 10^4. \end{cases} \tag{4.6}$$

(a) The profiles of the phase field variable ϕ.

(b) The profiles of the temperature variable T.
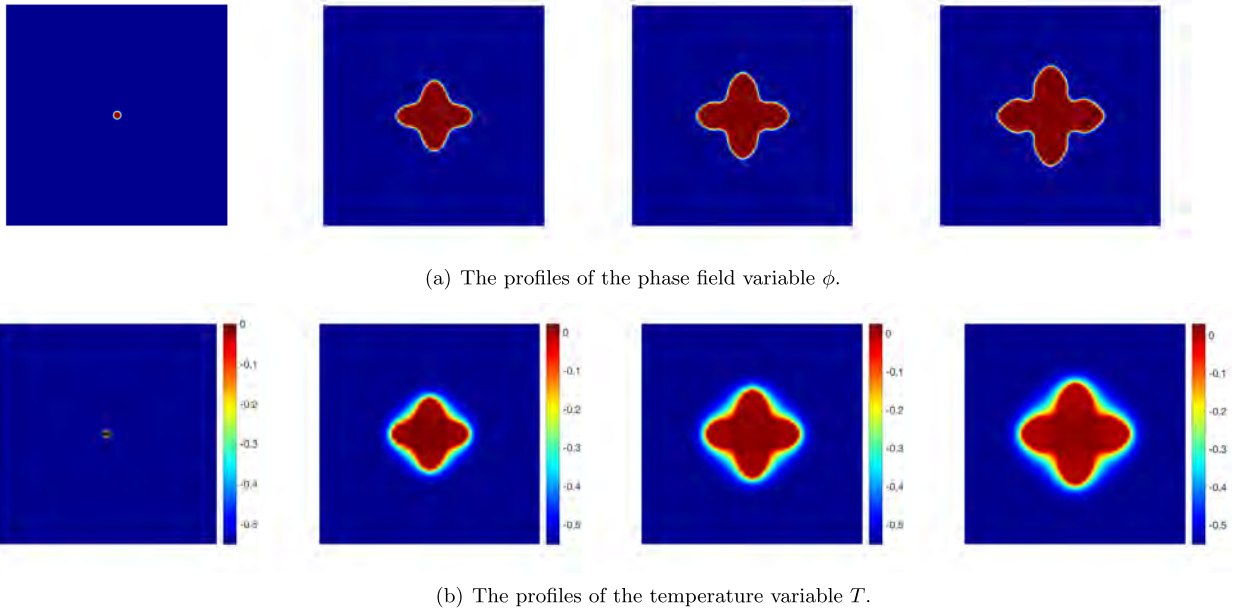
Fig. 4.3. The 2D dynamical evolution of dendritic crystal growth process when the flow fields are absent by using the weakly anisotropic strength parameter $\epsilon_4 = 0.01$, where (a) is the profiles for the phase field variable ϕ, and (b) is the profiles for the temperature T. Snapshots of the numerical approximation are taken at $t = 0, 100, 140$, and 180.

(a) The profiles of the phase field variable ϕ.

(b) The profiles of the temperature variable T.
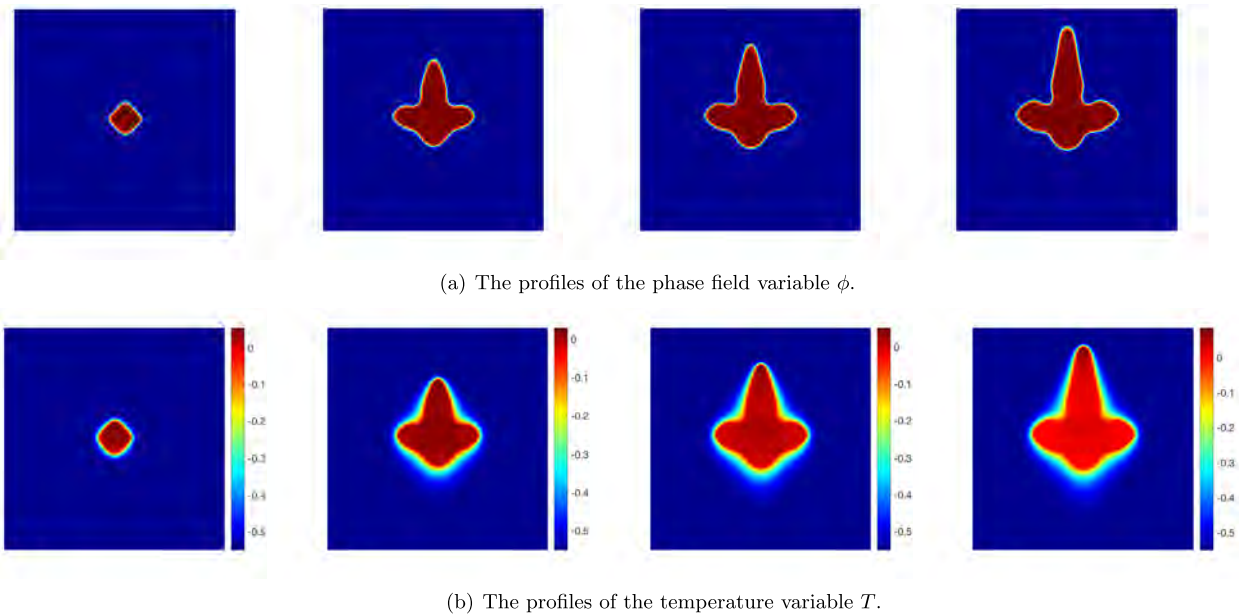
Fig. 4.4. The 2D dynamical evolution of dendritic crystal growth process when the flow fields are coupled by using the weakly anisotropic strength parameter $\epsilon_4 = 0.01$, where (a) is the profiles for the phase field variable ϕ, and (b) is the profiles for the temperature T. Snapshots of the numerical approximation are taken $t = 20, 60, 100, 120$, and 140.

Note these parameters are the rescaled values which are in the rough range of the parameters provided by [29,31,32,64]. We next perform a series of simulations with the fourfold anisotropic by varying the anisotropy strength ϵ_4. In all simulations, we use the time step $\delta t = 0.01$.

We first set a weak anisotropic strength as $\epsilon_4 = 0.01$. In Fig. 4.3(a), snapshots of the phase variable ϕ are shown at various times when the flow field are absent by setting $\mathbf{u} \equiv \mathbf{0}$ in (3.5). The tiny circle at the initial moment $t = 0$, shown in the first subfigure in Fig. 4.3(a), works as a crystal nucleus to grow with the time. Due to the anisotropic effects, we then observe the growth of the crystalline phase that finally becomes an anisotropic shape with four protrusive branches.

(a) The profiles of the phase field variable ϕ.

(b) The profiles of the temperature variable T.
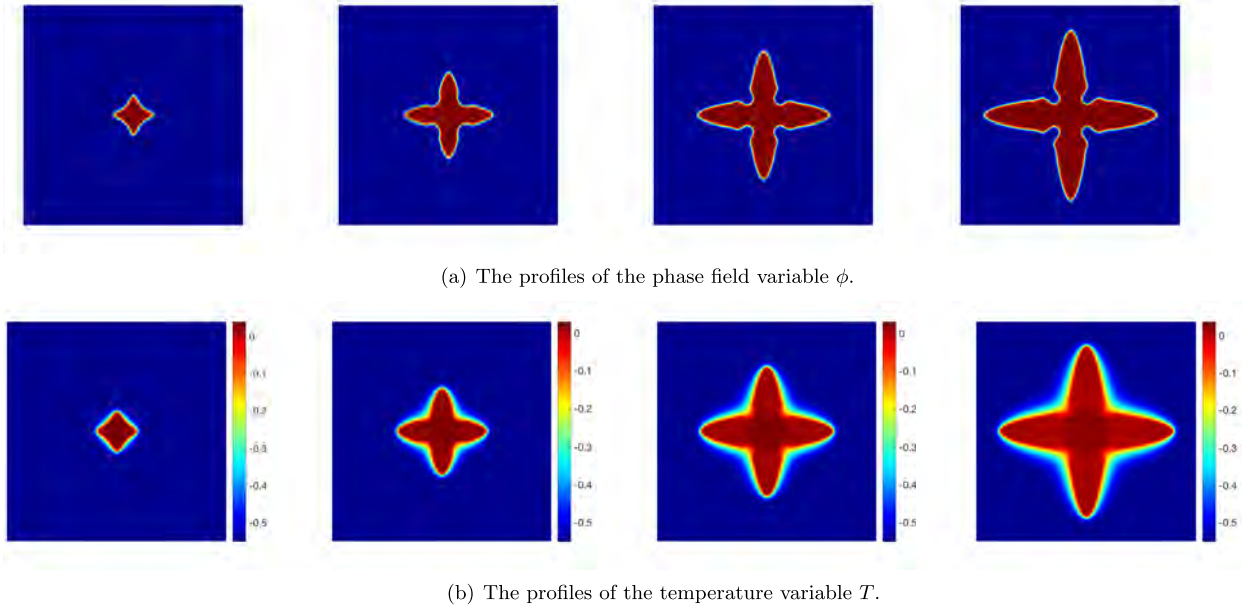
Fig. 4.5. The 2D dynamical evolution of dendritic crystal growth process when the flow fields are absent by using the moderate anisotropic strength parameter $\epsilon_4 = 0.03$, where (a) is the profiles for the phase field variable ϕ and (b) is the profiles for the temperature T. Snapshots of the numerical approximations are taken $t = 20, 60, 100$, and 140.

(a) The profiles of the phase field variable ϕ.

(b) The profiles of the temperature variable T.
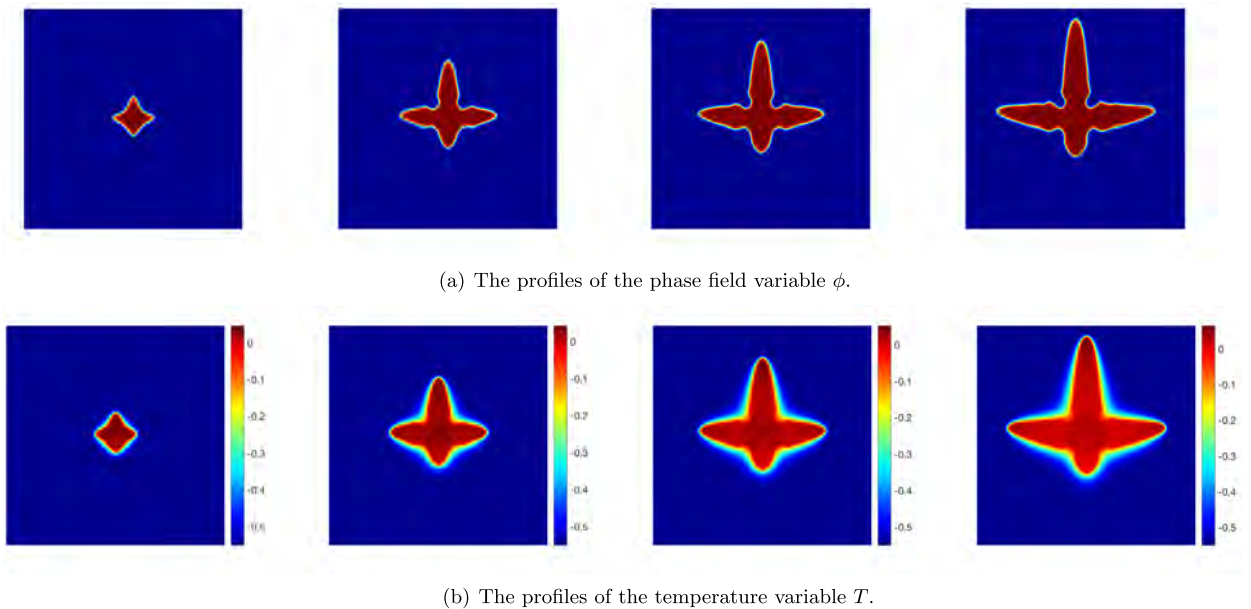
Fig. 4.6. The 2D dynamical evolution of dendritic crystal growth process when the flow fields are coupled, by using the moderate anisotropic strength parameter $\epsilon_4 = 0.03$, where (a) is the profiles for the phase field variable ϕ, and (b) is the profiles for the temperature T. Snapshots of the numerical approximation are taken $t = 20, 60, 80$, and 100.

In Fig. 4.3(b), we show the profiles of the temperature field T, that agrees well with the phase field variable ϕ due to the latent heat coupling terms.

In Fig. 4.4, we show snapshots of the phase variable ϕ at various times for the flow coupled case. We observe that the growth speed of the upstream tip with flow is much higher than that without flow because the impinging flow reduces the thermal boundary-layer thickness on the upstream side (cf. [2,48]). For example, when $t = 140$, the upstream tip with flow almost touches the upper domain boundary, but the distance that the upstream tip without flow travels is just half of that with flow. The growth speed of the downstream tip performs the opposite, i.e., it grows more slowly than that without flow because of advection of heat from the upstream portion of the dendrite. An interesting observation is that the horizontal

(a) The profiles of the phase field variable ϕ.

(b) The profiles of the temperature variable T.
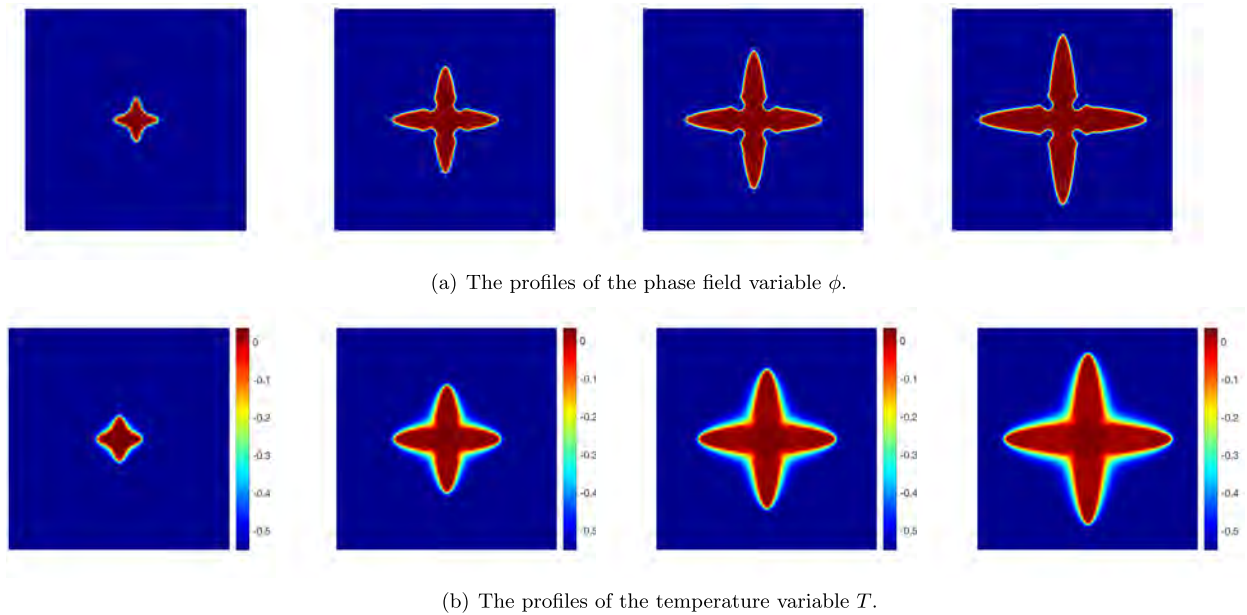
Fig. 4.7. The 2D dynamical evolution of dendritic crystal growth process when the flow fields are absent by using the strongly anisotropic strength parameter $\epsilon_4 = 0.05$, where (a) is the profiles for the phase field variable ϕ, and (b) is the profiles for the temperature T. Snapshots of the numerical approximation are taken $t = 20, 60, 80$, and 100.

(a) The profiles of the phase field variable ϕ.

(b) The profiles of the temperature variable T.
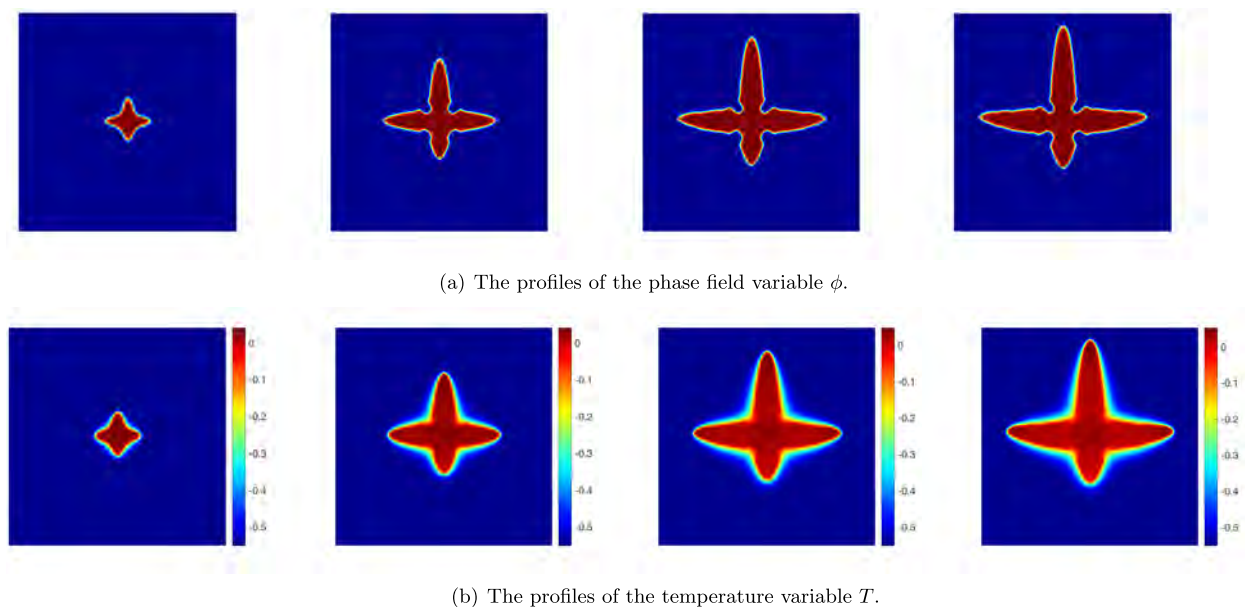
Fig. 4.8. The 2D dynamical evolution of dendritic crystal growth process when the flow fields are coupled, by using the strongly anisotropic strength parameter $\epsilon_4 = 0.05$, where (a) is the profiles for the phase field variable ϕ, and (b) is the profiles for the temperature T. Snapshots of the numerical approximation are taken $t = 20, 60, 80$, and 90.

tips grow slightly upwards that present the *tilting* shape, which is due to the asymmetry of the heat fluxes on the upper and lower sides of the horizontal arm (cf. [48]). The profiles of the temperature field T for the flow coupled case are shown in Fig. 4.3(b) as well.

Next, we set the anisotropic strength to be a moderate value of $\epsilon_4 = 0.03$. In Fig. 4.5 and Fig. 4.6, we show the evolution of the phase variable ϕ and temperature field T for the no flow case and flow coupled case, respectively. Comparing to the weak anisotropy case shown in Fig. 4.3 and Fig. 4.4, we observe that the four protrusion branches become more slender remarkably. This means the thickness of formed branches can be affected by the magnitude of ϵ_4, and larger value of ϵ_4 can bring more slender pattern of branches. Moreover, similar to the weak anisotropy case, the upstream tip grows much
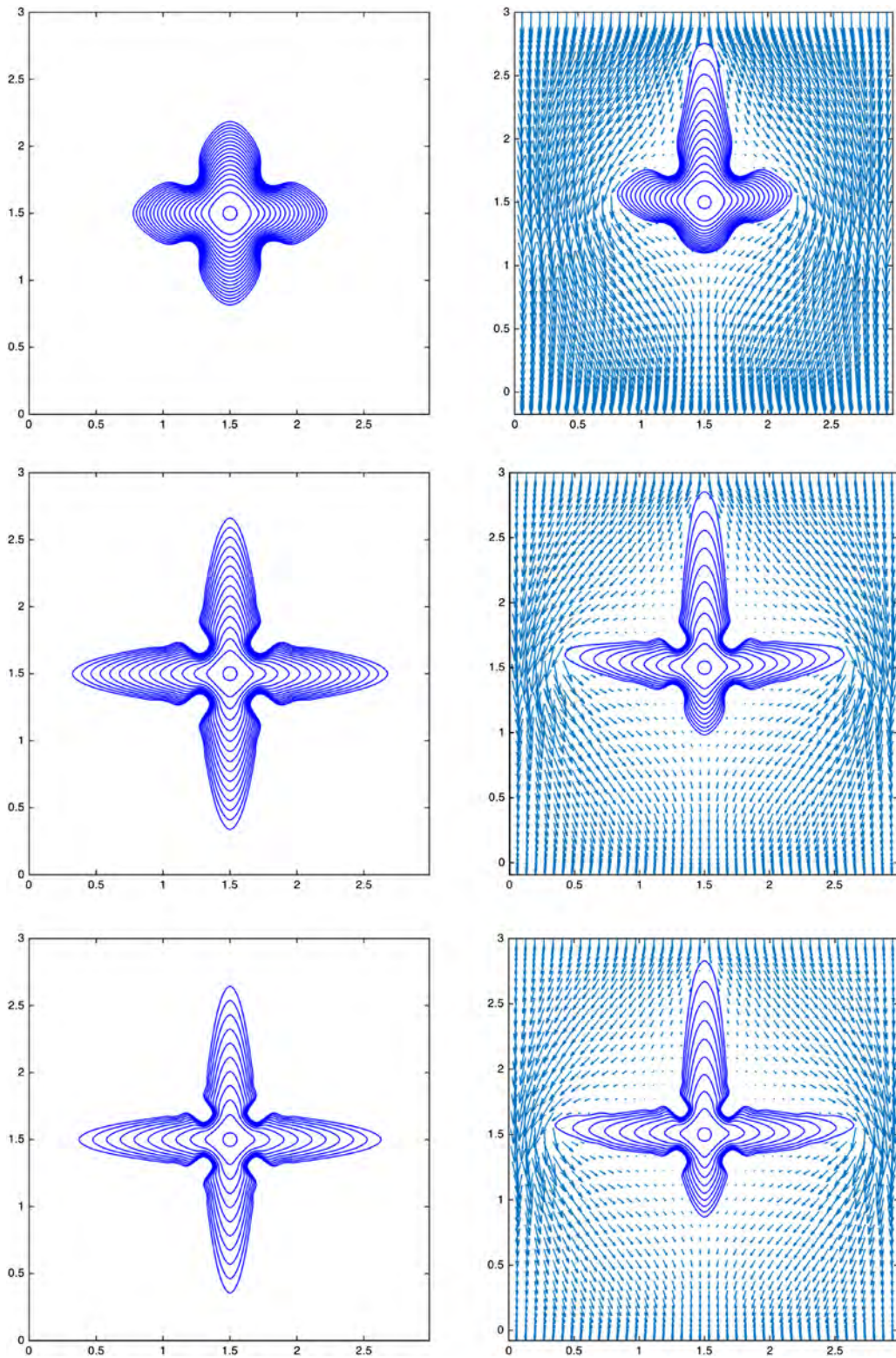
Fig. 4.9. The summary of the contour of the interface $\{\phi = 0\}$ every 10 time units from the initial moment for the three anisotropy strengths without flow (left panel), and with flow (right panel), where, $\epsilon_4 = 0.01$ (top panel), $\epsilon_4 = 0.03$ (middle panel), and $\epsilon_4 = 0.05$ (bottom panel). For the flow coupled case, the flow fields are interpolated for the better visualization.

(a) Original B-SPF model. (b) Modified model. (c) Comparisons at $t = 90$.
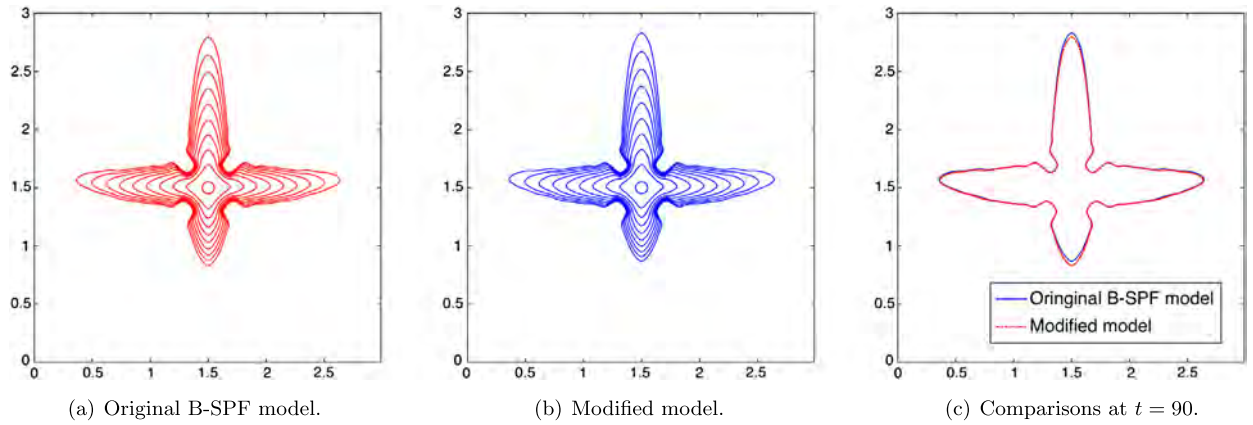
Fig. 4.10. The comparisons between the original B-SPF model (2.14)-(2.9)-(2.5)-(2.10) and the modified model (2.8)-(2.9)-(2.5)-(2.10) for the flow coupled case, where the contours of the interface $\{\phi = 0\}$ every 10 time units from the initial moment are plotted, the original B-SPF model (left), modified model (middle), and their detailed comparisons at $t = 90$ (right). In both computations, we set $\epsilon_4 = 0.05$.

(a) log(Energy) with the time. (b) Radius with the time.
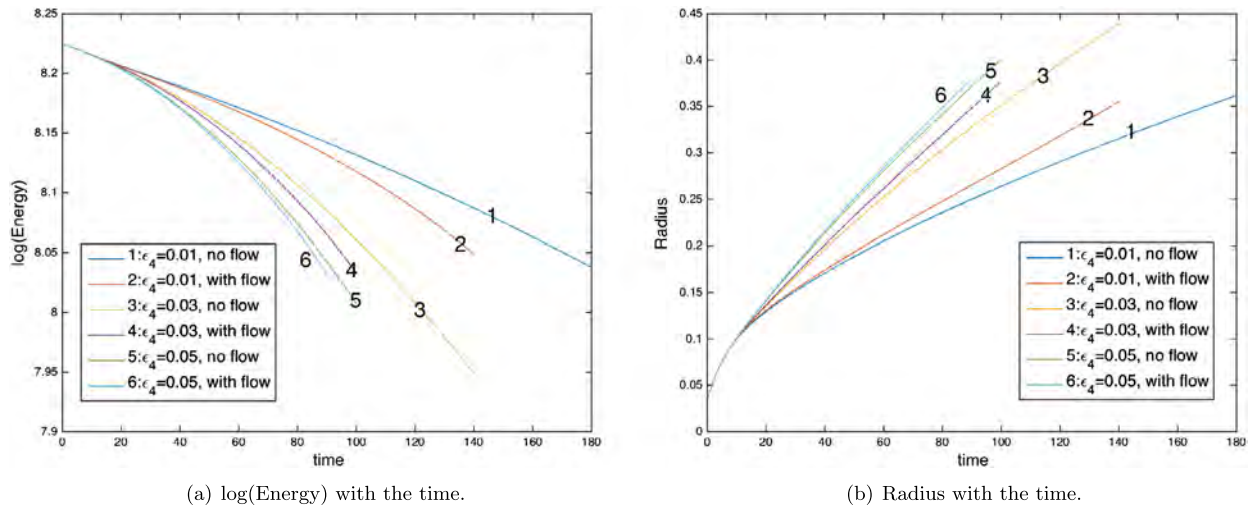
Fig. 4.11. (a) Time evolutions of the logarithm of the free energy functional for the 2D fourfold examples with three different anisotropy strengths $\epsilon_4 = 0.01$, 0.03, and 0.05, for the flow absent and flow coupled cases; (b) The size of the dendritic crystals changing with time, where the crystal size is measured by an equivalent radius of a circle with the same area.

more quickly than that of no flow case, while the downstream tip grows more slowly than that of no flow case. We also observe that the tilting shape appears for the two horizontal arms. The profiles of the temperature field T for the no flow case and flow coupled case are shown in Fig. 4.5(b) and Fig. 4.6(b), respectively.

Finally, we perform the simulations by using a strong anisotropy parameter as $\epsilon_4 = 0.05$ in Fig. 4.7 and Fig. 4.8 for the no flow case and flow coupled case, respectively. The hypothesis that larger ϵ_4 lead to more slender branches are proven once again, that can be easily observed by comparing Fig. 4.5(b) with Fig. 4.7(b), and Fig. 4.6(b) with Fig. 4.8(b). Meanwhile, the growth speed of the upstream and downstream tips are still similar as the two previous cases. The tilting shape appears on the horizontal arms are observed too.

To get more detailed evolution of the dendrites, in Fig. 4.9, we summarize the contour of the interface $\{\phi = 0\}$ every 10 time units from the initial moment for the above three anisotropy strengths without flow (top panel), and with flow (bottom panel). For the better visualization, we have interpolated the flow field onto a grid that is about 6 times coarser than the one used in the computations. It can be seen that the shape of the dendrites is significantly influenced by the flow. When the flow field is coupled, the growth velocities of the upstream tips are much higher than those of the downstream tips and the horizontal tips. All these numerical results demonstrate similar features to those obtained in the computations of Beckerman et al. in [2,48].

We further compare the computed results by using the original B-SPF model (2.14)-(2.9)-(2.5)-(2.10) and the modified model (2.8)-(2.9)-(2.5)-(2.10) for the flow coupled case. In both simulations, we use the same anisotropic strength $\epsilon_4 = 0.05$ and the flow is coupled therein. In Fig. 4.10(a) and (b), we summarize the contour of the interface $\{\phi = 0\}$ every 10 time
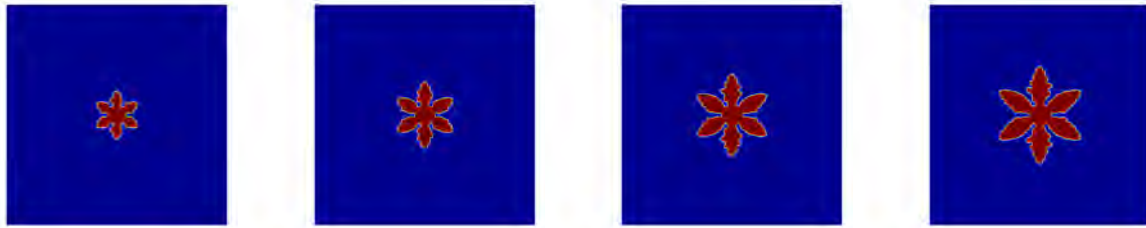
(a) The profiles of the phase field variable ϕ.
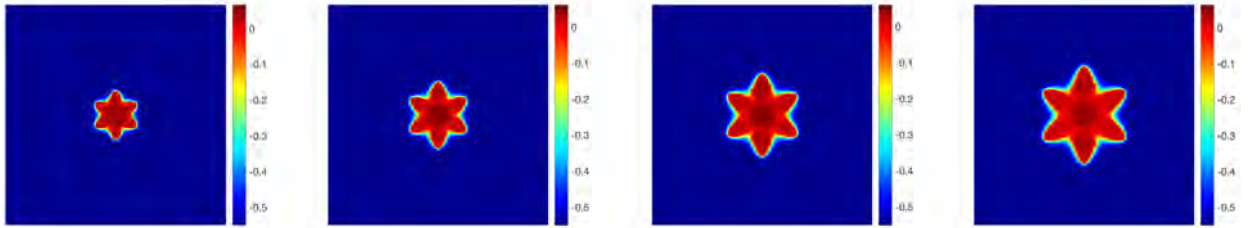
(b) The profiles of the temperature variable T.

Fig. 4.12. The 2D dynamical evolution of dendritic crystal growth process when the flow fields are absent, by using the sixfold anisotropy, the linear kinetic coefficient $\lambda = 355$, and other parameters specified in (4.8), where (a) is the profiles for the phase field variable ϕ, and (b) is the profiles for the temperature T. Snapshots of the numerical approximation are taken $t = 60, 100, 140$, and 180.
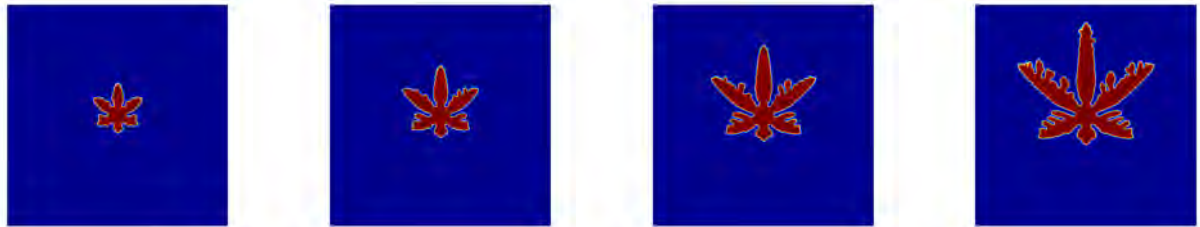
(a) The profiles of the phase field variable ϕ.
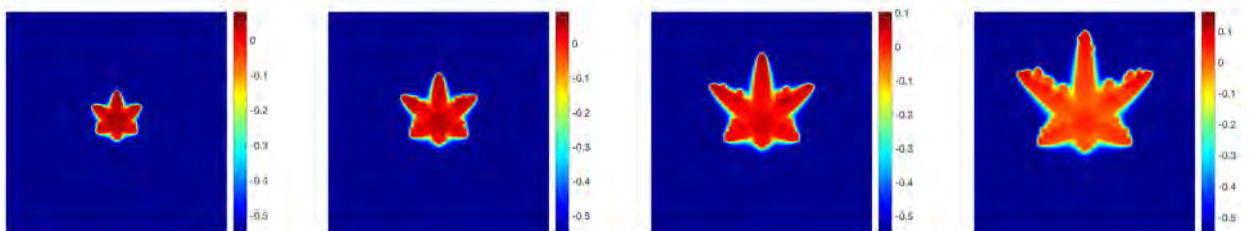
(b) The profiles of the temperature variable T.

Fig. 4.13. The 2D dynamical evolution of dendritic crystal growth process when the flow fields are coupled, by using the sixfold anisotropy, the linear kinetic coefficient $\lambda = 355$, and other parameters specified in (4.8), where (a) is the profiles for the phase field variable ϕ and (b) is the profiles for the temperature T. Snapshots of the numerical approximation are taken $t = 60, 100, 140$, and 180.

units for these two models respectively, and we find that no visible differences are noticeable. A more detailed comparison for the interfaces at $t = 90$ is given in Fig. 4.10(c).

In Fig. 4.11, we summarize the evolutions of the logarithm of the total free energy which monotonically decay and the radius of the crystal that is measured by an equivalent radius of a circle with the same area. When the flow field is present, we observe that the total energy decays faster, and the radius or area of the dendrites grows faster than those of the no flow case.

(a) The profiles of the phase field variable ϕ.

(b) The profiles of the temperature variable T.

Fig. 4.14. The 2D dynamical evolution of dendritic crystal growth process when the flow fields are absent, by using the sixfold anisotropy, the linear kinetic coefficient $\lambda = 380$, and other parameters specified in (4.8), where (a) is the profiles for the phase field variable ϕ and (b) is the profiles for the temperature T. Snapshots of the numerical approximation are taken $t = 40, 80, 120$, and 160.

(a) The profiles of the phase field variable ϕ.

(b) The profiles of the temperature variable T.
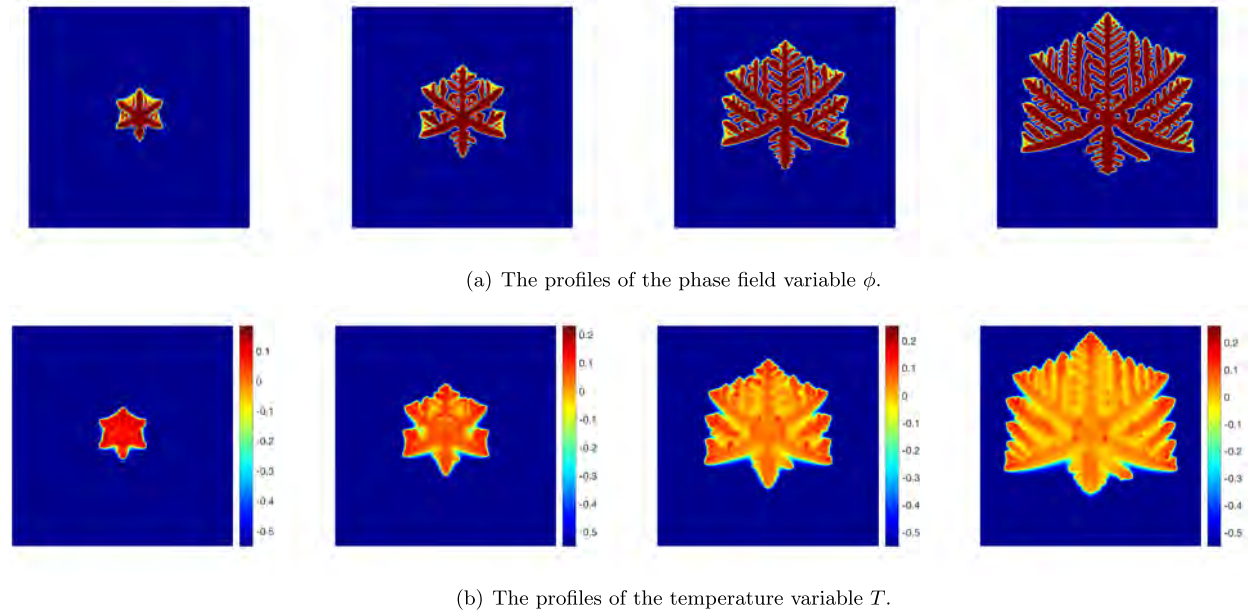
Fig. 4.15. The 2D dynamical evolution of dendritic crystal growth process when the flow fields are coupled, by using the sixfold anisotropy, the linear kinetic coefficient $\lambda = 380$, and other parameters specified in (4.8), where (a) is the profiles for the phase field variable ϕ and (b) is the profiles for the temperature T. Snapshots of the numerical approximation are taken $t = 40, 80, 120$, and 160.

4.4. 2D dendrite crystal growth with sixfold anisotropy

In this subsection, we investigate how the sixfold anisotropy can affect the shape of the dendritic crystal by setting $m = 6$ in (2.2). We use the same initial condition (4.5), and the same boundary conditions specified in (4.3) but setting

$$v|_{(y=0, \, y=L_2)} = -0.02. \tag{4.7}$$
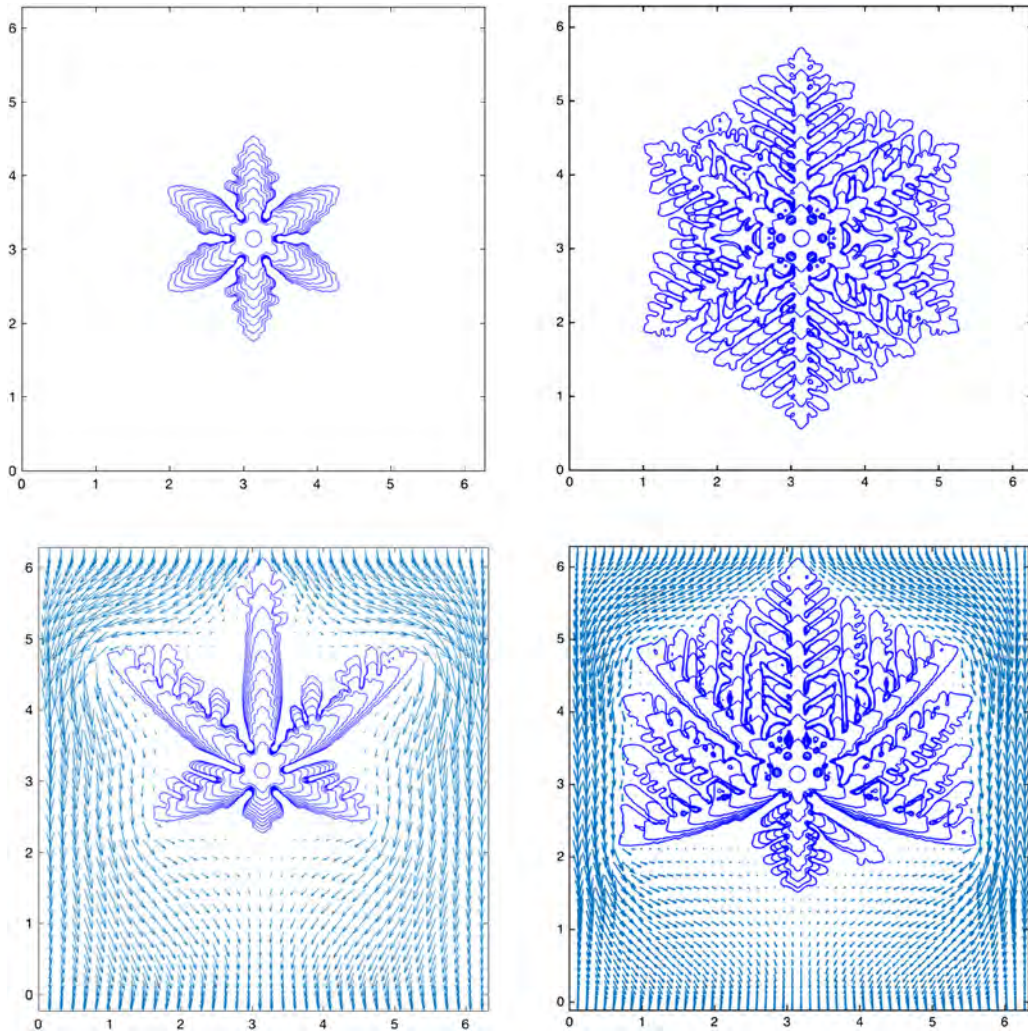
Fig. 4.16. The summary of the contour of the interface $\{\phi = 0\}$ every 20 time units since the initial moment for the sixfold anisotropy, without flow (top panel), and with flow (bottom panel). $\lambda = 355$ (left panel), $\lambda = 380$ (right panel). For the flow coupled case, the flow fields are interpolated for the better visualization.

The order parameters are set as follows,

$$
\begin{cases}
L_1 = L_2 = 2\pi, N = 801, M = 800, \\
\tau = 4268.4, \epsilon_4 = 0.05, \epsilon = 0.0112, D = 0.000225, \\
K = 0.75, S_1 = S_2 = 4, \nu = 1, h = 0.01, B = 5 \times 10^4.
\end{cases}
\tag{4.8}
$$

We perform a series of simulations by varying the linear kinetic coefficient λ. In all simulations, we use the time step $\delta t = 0.01$.

First, to be consistent with the fourfold case, we still set $\lambda = 355$. In Fig. 4.12, we present the dynamics of the phase variable and temperature field for the no flow case. We observe that the initial circular nucleus grows into six main branches when time evolves. Moreover, on each main branch, some tiny protrusions appear. We further perform simulations for the flow coupled case. In Fig. 4.13(a), snapshots of the phase variable at various times are presented, in which we observe, (i) the growth speed of the upstream, upper right, upper left tips are much higher than that without flow; (ii) the growth speed of the lower right and lower left tips grow almost the same as that without flow; (iii) the growth speed of the downstream grows much slowly than that without flow; (iv) the tilting phenomenon appears on the upper right, upper left, lower right, and lower left arms.

We further set the kinetic coefficient $\lambda = 380$ and fix all other parameters. In Fig. 4.14(a), for the flow absent case, the snapshots of the phase field variable are shown, where we observe that plenty of tiny protrusions form on each main branch, and the initial circular nucleus grows to a snowflake pattern finally. Similar snowflake patterns had been reported in [32] using a slightly different model. The temperature field is presented in Fig. 4.14(b). When the flow field is coupled, the

(a) log(Energy) with the time.   (b) Radius with the time.
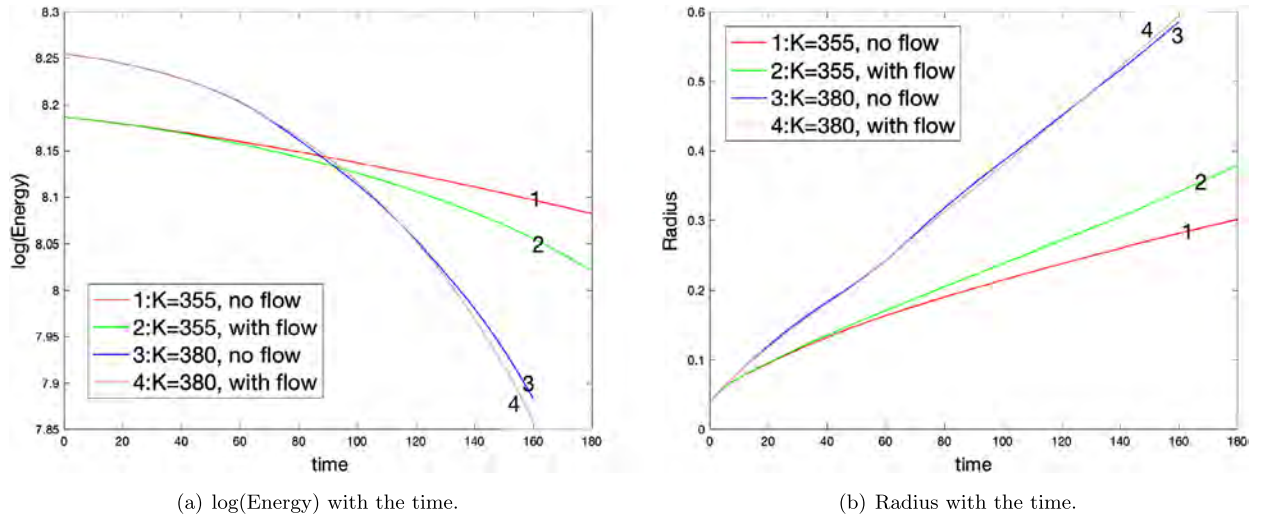
Fig. 4.17. (a) Time evolutions of the logarithm of the free energy functional for the 2D sixfold examples with two different linear kinetic coefficients $\lambda = 355$ and $\lambda = 380$, for the flow absent and flow coupled cases; (b) The size of the dendritic crystals changing with time where the crystal size is measured by an equivalent radius of a circle with the same area.

patterns of the phase field variable and temperature field are shown in Fig. 4.15(a) and (b), respectively. Since the growth speed of six tips, and the tilting shape all follow the same line as the previous case, it is unnecessary to go into details.

In Fig. 4.16, we summarize the contour of the interface $\{\phi = 0\}$ every 20 time units from the initial moment for the above two cases without flow (top panel), and with flow (bottom panel). For the better visualization, we have interpolated the flow field onto a grid that is about 12 times coarser than the one used in the computations. In Fig. 4.17, we summarize the evolutions of the logarithm of the total free energy which mono-tonically decay and the radius of the crystal. Similar as the fourfold case, when the flow field is coupled, the total free energy decays faster, and the radius or area of the dendrites grows faster than those of the no flow case.

5. Concluding remarks

We studied in this paper a dendritic solidification phase field that involves melt convections in the liquid phase. We first reformulate the momentum equation in Beckerman's model into a form which is suitable for numerical approximations and derived the associated energy dissipation law. We then construct an efficient time marching scheme by combining the modified pressure-correction method and the stabilized-IEQ method. The scheme enjoys the following properties: (i) it leads to three decoupled linear systems to solve at each time step, and (ii) it is unconditionally stable and obeys a discrete energy law. Hence, the obtained numerical scheme is extremely efficient. To the author's knowledge, this is the first unconditionally energy stable scheme for the flow coupled anisotropic phase field dendritic model, that can decouple the phase function, temperature, velocity, and pressure, and lead to linear decoupled elliptic equations, at each time step. We further numerically verify the accuracy in time and present various numerical results for some benchmark numerical simulations. While we have considered only time discretizations here, the results can carry over to any consistent finite-dimensional Galerkin approximations (finite elements or spectral), since the proofs are all based on variational formulations with all test functions in the same space as the trial function.

It is remarkable that the numerical work about the dendritic model is still on early stage and there remain many potential research topics concerning the modeling, analysis, and simulations. For example, an obvious topic is how to derive the rigorous error analysis for the proposed scheme, in the context of the semi-discrete in time or fully-discrete in space and time. Meanwhile, note the proposed scheme in this paper is just first-order accurate in time, thus how to develop an energy stable scheme while preserving the second-order accuracy in time will be another challenging and meaningful topic. It is also unclear but possible to develop a fully decoupled scheme that can decouple the computations of the phase field variable from the temperature. We notice that there are many interests focusing on the numerical simulations of atomic crystal evolving with dendritic tips (cf. [47]), which requires to develop a seamless model that can couple the dendritic phase-field model with the so-called phase-field crystal free energy [10], that could be another challenging topic of modeling and algorithm developments. The model in this paper only considers the dendritic solidification for the pure material, thus an interesting but very challenging research topic is how to develop an efficient scheme to solving the binary alloy dendritic solidification model which couples the hydrodynamics, phase field variable, concentration field for solvents, as well as the heat transfer.

References

[1] R. Ananth, W.N. Gill, Dendritic growth of an elliptical paraboloid with forced convection in the melt, J. Fluid Mech. 28 (1989) 575–593.
[2] C. Beckermann, H.-J. Diepers, I. Steinbach, A. Karma, X. Tong, Modeling melt convection in phase-field simulations of solidification, J. Comput. Phys. 154 (1999) 468–496.
[3] C.C. Chen, Y.L. Tsai, C.W. Lan, Adaptive phase field simulation of dendritic crystal growth in a forced flow: 2D vs. 3D morphologies, Int. J. Heat Mass Transf. 52 (2009) 1158–1166.
[4] L. Chen, J. Zhao, X. Yang, Regularized linear schemes for the molecular beam epitaxy model with slope selection, Appl. Numer. Math. 128 (2018) 139–156.
[5] M-W. Chen, X-F. Wang, Z-D. Wang, J-X. Xie, Dendritic growth from a binary system in an external flow: steady state solution with zero surface tension, J. Cryst. Growth 310 (2008) 655–664.
[6] J.B. Collins, H. Levine, Diffuse interface model of diffusion-limited crystal growth, Phys. Rev. B 31 (1985) 6119.
[7] S.R. Coriell, W.J. Boettinger, M.R. Cordes, R.F. Sekerka, Effect of gravity on coupled convective and interfacial instabilities during directional solidification, Adv. Space Res. 1 (1981) 5–11.
[8] S.H. Davis, Hydrodynamic interactions in directional solidification, J. Fluid Mech. 212 (1990) 241.
[9] A.E. Diegel, S.W. Walker, A finite element method for a phase field model of nematic liquid crystal droplets, Commun. Comput. Phys. 25 (2019) 155–188.
[10] K.R. Elder, Mark Katakowski, Mikko Haataja, Martin Grant, Modeling elasticity in crystal growth, Phys. Rev. Lett. 88 (24) (2002) 245701.
[11] D.J. Eyre, Unconditionally gradient stable time marching the Cahn-Hilliard equation, in: Computational and Mathematical Models of Microstructural Evolution, San Francisco, CA, 1998, in: Mater. Res. Soc. Symp. Proc., vol. 529, 1998, pp. 39–46.
[12] X. Feng, Y. He, C. Liu, Analysis of finite element approximations of a phase field model for two-phase fluids, Math. Comput. 76 (258) (2007) 539–571.
[13] H.S. Furtadoa, A.T. Bernardesb, R.F. Machadob, C.A. Silva, Numerical simulation of solute trapping phenomena using phase-field solidification model for dilute binary alloys, Mater. Res. 12 (2009) 345–351.
[14] Y. Gao, X. He, L. Mei, X. Yang, Fully decoupled, linearized, and energy stable finite element method for Cahn-Hilliard-Navier-Stokes-Darcy model, SIAM J. Sci. Comput. 40 (2018) B110–B137.
[15] M.E. Glicksman, R.J. Schaefer, J.D. Ayers, Dendritic growth-a test of theory, Metall. Trans. A 7 (1976) 1747–1759.
[16] H. Gomez, T.J.R. Hughes, Provably unconditionally stable, second-order time-accurate, mixed variational methods for phase-field models, J. Comput. Phys. 230 (2011) 5310–5327.
[17] B. Gonzalez-Ferreiro, H. Gomez, I. Romero, A thermodynamically consistent method for a phase-field model of solidification, Commun. Nonlinear Sci. Numer. Simul. 19 (2014) 2309–2323.
[18] J.L. Guermond, P. Minev, J. Shen, An overview of projection methods for incompressible flows, Comput. Methods Appl. Mech. Eng. 195 (2006) 6011–6045.
[19] R. Guo, Y. Xu, A high order adaptive time-stepping strategy and local discontinuous Galerkin method for the modified phase field crystal equation, Commun. Comput. Phys. 24 (2018) 123–151.
[20] B.I. Halperin, P.C. Hohenberg, S.-K. Ma, Renormalization-group methods for critical dynamics: I. Recursion relations and effects of energy conservation, Phys. Rev. B 139 (10) (1974).
[21] D. Han, A. Brylev, X. Yang, Z. Tan, Numerical analysis of second order, fully discrete energy stable schemes for phase field models of two phase incompressible flows, J. Sci. Comput. 70 (2017) 965–989.
[22] H. Haruo, S. Yasuji, Quantitative measurements on the morphology of a NH4Br dendritic crystal growth in a capillary, J. Cryst. Growth 58 (1982) 297–303.
[23] Y. He, Y. Liu, T. Tang, On large time-stepping methods for the Cahn-Hilliard equation, Appl. Numer. Math. 57 (2007) 616–628.
[24] Q. Huang, X. Yang, X. He, A linear, decoupled and energy stable scheme for smectic-a liquid crystal flows, Discrete Contin. Dyn. Syst., Ser. B 23 (2018) 2177–2192.
[25] S.C. Huang, M.E. Glicksman, Fundamentals of dendritic solidification I and II, Acta Metall. 29 (1981) 701–734.
[26] J. Bosch, C. Kahle, M. Stoll, Preconditioning of a coupled Cahn-Hilliard Navier-Stokes system, Commun. Comput. Phys. 23 (2018) 603–628.
[27] J.-H. Jeong, J.A. Dantzig, N. Goldenfeld, Dendritic growth with fluid flow in pure materials, Metall. Mater. Trans. A 34 (2003) 459–466.
[28] J.-H. Jeong, N. Goldenfeld, J.A. Dantzig, Phase field model for three-dimensional dendritic growth with fluid flow, Phys. Rev. E 55 (2001) 041602.
[29] A. Karma, A.E. Lobkovsky, Unsteady crack motion and branching in a phase-field model of brittle fracture, Phys. Rev. Lett. 92 (2004) 245510.
[30] A. Karma, W. Rappel, Quantitative phase-field modeling of dendritic growth in two and three dimensions, Phys. Rev. E 57 (1998) 4323–4349.
[31] A. Karma, W. Rappel, Phase-field model of dendritic sidebranching with thermal noise, Phys. Rev. E 60 (1999) 3614–3625.
[32] R. Kobayashi, Modeling and numerical simulations of dendritic crystal growth, Physica D 63 (1993) 410.
[33] Q. Li, C. Beckermann, Modeling of free dendritic growth succinitrile-acetone alloys with thermosolutal melt convection, J. Cryst. Growth 236 (2002) 482–498.
[34] Y. Li, J. Kim, Phase-field simulations of crystal growth with adaptive mesh refinement, Int. J. Heat Mass Transf. 55 (2012) 7926–7932.
[35] Y. Li, H. Lee, J. Kim, A fast robust and accurate operator splitting method for phase field simulations of crystal growth, J. Cryst. Growth 321 (2011) 176–182.
[36] E. Meca, V. Shenoy, J. Lowengrub, Phase field modeling of two dimensional crystal growth with anisotropic diffusion, Phys. Rev. E 88 (2013) 052409.
[37] A. Moure, H. Gomeze, Three-dimensional simulation of obstacle-mediated chemotaxis, Biomech. Model. Mechanobiol. 17 (2018) 1243–1268.
[38] B. Nestler, D. Danilov, P. Galenko, Crystal growth of pure substances: phase field simulations in comparison with analytical and experimental results, J. Comput. Phys. 207 (2005) 221–239.
[39] H. Neumann-Heyme, K. Eckert, S. Odenbach, Free dendrite growth under modulated flow in pure substances: two-dimensional phase-field simulations, IOP Conf. Ser., Mater. Sci. Eng. 27 (2012) 012045.
[40] M. Plapp, A. Karma, Multiscale finite-difference-diffusion-Monte-Carlo method for simulating dendritic solidification, J. Comput. Phys. 165 (2000) 592–619.
[41] N. Provatas, N. Goldenfeld, J. Dantzig, Efficient computation of dendritic microstructures using adaptive mesh refinement, Phys. Rev. Lett. 80 (1998) 3308–3311.
[42] J.C. Ramirez, C. Beckermann, A. Karma, H.-J. Diepers, Phase-field modeling of binary alloy solidification with coupled heat and solute diffusion, Phys. Rev. E 69 (2004) 051607.
[43] J. Shen, Efficient spectral-Galerkin method I. Direct solvers for second- and fourth-order equations by using Legendre polynomials, SIAM J. Sci. Comput. 15 (1994) 1489–1505.
[44] J. Shen, J. Xu, Stabilized predictor-corrector schemes for gradient flows with strong anisotropic free energy, Commun. Comput. Phys. 24 (2018) 635–654.
[45] J. Shen, X. Yang, Numerical approximations of Allen-Cahn and Cahn-Hilliard equations, Discrete Contin. Dyn. Syst., Ser. A 28 (2010) 1669–1691.
[46] J. Shen, X. Yang, A phase-field model and its numerical approximation for two-phase incompressible flows with different densities and viscosities, SIAM J. Sci. Comput. 32 (2010) 1159–1179.

[47] S. Tang, J. Wang, J. Li, Z. Wang, Y. Guo, C. Guo, Y. Zhou, Phase-field-crystal investigation of the morphology of a steady-state dendrite tip on the atomic scale, Phys. Rev. E 95 (2017) 062803.
[48] X. Tong, C. Beckermann, A. Karma, Q. Li, Phase-field simulations of dendritic crystal growth in a forced flow, Phys. Rev. E 63 (2001) 061601.
[49] R. Trivedi, W. Kurz, Dendritic growth, Int. Mater. Rev. 39 (1994) 49.
[50] S.-L. Wang, R.F. Sekerka, A.A. Wheeler, B.T. Murray, S.R. Coriell, R.J. Braun, G.B. McFadden, Thermodynamically-consistent phase-field models for solidi-fication, Physica D 69 (1993) 189–200.
[51] J.A. Warren, W.J. Boettinger, Prediction of dendritic growth and microsegregation patterns in a binary alloy using the phase field method, Acta Metall. Mater. 43 (1995) 689–703.
[52] C. Xu, T. Tang, Stability analysis of large time-stepping methods for epitaxial growth models, SIAM J. Numer. Anal. 44 (2006) 1759–1779.
[53] J.J. Xu, Dendritic growth from a melt in an external flow: uniformly valid asymptotic solution for the steady state, J. Fluid Mech. 263 (1994) 227–244.
[54] Y. Yan, W. Chen, C. Wang, S.M. Wise, A second-order energy stable BDF numerical scheme for the Cahn-Hilliard equation, Commun. Comput. Phys. 23 (2018) 572–602.
[55] X. Yang, Error analysis of stabilized semi-implicit method of Allen-Cahn equation, Discrete Contin. Dyn. Syst., Ser. B 11 (4) (2009) 1057–1070.
[56] X. Yang, Linear, first and second order and unconditionally energy stable numerical schemes for the phase field model of homopolymer blends, J. Comput. Phys. 327 (2016) 294–316.
[57] X. Yang, Efficient linear, stabilized, second-order time marching schemes for an anisotropic phase field dendritic crystal growth model, Comput. Meth-ods Appl. Mech. Eng. 347 (2019) 316–339.
[58] X. Yang, L. Ju, Efficient linear schemes with unconditionally energy stability for the phase field elastic bending energy model, Comput. Methods Appl. Mech. Eng. 315 (2017) 691–712.
[59] X. Yang, L. Ju, Linear and unconditionally energy stable schemes for the binary fluid-surfactant phase field model, Comput. Methods Appl. Mech. Eng. 318 (2017) 1005–1029.
[60] X. Yang, H. Yu, Efficient second order unconditionally stable schemes for a phase field moving contact line model using an invariant energy quadrati-zation approach, SIAM J. Sci. Comput. 40 (2018) B889–B914.
[61] X. Yang, G-D. Zhang, Numerical approximations of the Cahn-Hilliard and Allen-Cahn equations with general nonlinear potential using the invariant energy quadratization approach, 2018, submitted for publication, arXiv:1712.02760.
[62] X. Yang, J. Zhao, X. He, Linear, second order and unconditionally energy stable schemes for the viscous Cahn-Hilliard equation with hyperbolic relax-ation using the invariant energy quadratization method, J. Comput. Appl. Math. 343 (2018) 80–97.
[63] X. Yang, J. Zhao, Q. Wang, J. Shen, Numerical approximations for a three components Cahn-Hilliard phase-field model based on the invariant energy quadratization method, Math. Models Methods Appl. Sci. 27 (2017) 1993–2030.
[64] J. Zhao, Q. Wang, X. Yang, Numerical approximations for a phase field dendritic crystal growth model based on the invariant energy quadratization approach, Int. J. Numer. Methods Eng. 110 (2017) 279–300.
[65] M-F. Zhu, T. Dai, S-Y. Lee, C-P. Hong, Modeling of solutal dendritic growth with melt convection, Comput. Math. Appl. 55 (2008) 1620–1628.